nature cancer

ARTICLES

https://doi.org/10.1038/s43018-020-0071-1

Check for updates

Keap1 mutation renders lung adenocarcinomas dependent on *Slc33a1*

Rodrigo Romero[1,2,11], Francisco J. Sánchez-Rivera[1,2,9,11], Peter M. K. Westcott[1], Kim L. Mercer[1,3], Arjun Bhutkar[1], Alexander Muir[1,10], Tania J. González Robles[1], Swanny Lamboy Rodríguez[2], Laura Z. Liao[2], Sheng Rong Ng[1,2], Leanne Li[1], Caterina I. Colón[1], Santiago Naranjo[1,2], Mary Clare Beytagh[2], Caroline A. Lewis[4], Peggy P. Hsu[1,5,6], Roderick T. Bronson[7,8], Matthew G. Vander Heiden[1,2,6] and Tyler Jacks[1,2,3] ✉

Approximately 20–30% of human lung adenocarcinomas (LUADs) harbor mutations in Kelch-like ECH-associated protein 1 (*KEAP1*) that hyperactivate the nuclear factor, erythroid 2-like 2 (*NFE2L2*) antioxidant program. We previously showed that *Kras*-driven *Keap1*-mutant LUAD is highly aggressive and dependent on glutaminolysis. Here we performed a druggable genome CRISPR screen and uncovered a *Keap1*-mutant-specific dependency on solute carrier family 33 member 1 (*Slc33a1*), as well as several functionally related genes associated with the unfolded protein response. Genetic and biochemical experiments using mouse and human *Keap1*-mutant tumor lines, as well as preclinical genetically engineered mouse models, validate *Slc33a1* as a robust *Keap1*-mutant-specific dependency. Furthermore, unbiased genome-wide CRISPR screening identified additional genes related to *Slc33a1* dependency. Overall, our study provides a rationale for stratification of patients harboring *KEAP1*-mutant or NRF2-hyperactivated tumors as likely responders to targeted SLC33A1 inhibition and underscores the value of integrating functional genetic approaches with genetically engineered mouse models to identify and validate genotype-specific therapeutic targets.

KEAP1, a negative regulator of *NFE2L2* (hereafter *NRF2*), is mutated in 20–30% of lung cancers[1–6]. NRF2 regulates a network of genes with antioxidant functions that mitigate oxidative damage via detoxification of reactive oxygen species (ROS) and xenobiotics, and regulation of glutathione (GSH) synthesis and recycling[2,7–10]. The high mutation frequency of *KEAP1/NRF2* suggests a critical role for this pathway and serves as a rationale for identifying new therapeutic strategies for this genetic subtype.

Inactivation of *Nrf2* in *Kras*-mutant genetically engineered mouse models (GEMMs) of pancreatic cancer and LUAD decreases tumor initiation and proliferation, suggesting that some RAS-driven tumors depend on NRF2 (refs. [11–13]). We recently showed that *Kras* and *Keap1* mutations cooperate to drive LUAD initiation and progression and that these tumors are sensitive to glutaminase inhibitors[14]. *KEAP1/NRF2*-mutant tumors have been shown to depend on nonessential amino acids and to increase pentose phosphate pathway flux and usage of glutamine-, serine- and cysteine-derived metabolites[15–19]. *KEAP1* mutations correlate with poor survival[1] and promote metastasis in *Keap1*-mutant GEMMs[20].

To investigate whether *Keap1*-mutant or otherwise NRF2-hyperactive tumors, harbored additional targetable dependencies, we performed a CRISPR screen targeting druggable genes in isogenic *Keap1*-mutant LUAD cells. Cross-validation with public CRISPR screening data uncovered several genotype-specific liabilities, including robust dependency on the endoplasmic reticulum (ER)-resident gene, *Slc33a1*. Using multiple approaches, including preclinical GEMMs of *Kras*-driven LUAD, we validated *Slc33a1* as a *Keap1*-mutant-specific dependency. Finally, we performed genome-wide modifier genetic screens to identify suppressors of *Slc33a1* dependency and highlight an underappreciated relationship between ER redox biology and *KEAP1* mutation in cancer. Altogether, these data implicate a vulnerability that could be therapeutically exploited in *KEAP1/NRF2*-mutant cancers.

Results

Druggable genome CRISPR screen identifies *Keap1*-mutant dependencies. We performed pooled CRISPR screens across two isogenic pairs of Cas9-expressing murine LUAD cell lines with $Kras^{G12D/+}$;$p53^{-/-}$ (KP) and $Kras^{G12D/+}$;$p53^{-/-}$;$Keap1^{-/-}$ (KPK) genotypes[14] (Fig. 1a,b) using a druggable genome library (DGL) targeting 4,915 genes with known or predicted druggability[21] (Fig. 1a,b, Extended Data Fig. 1a,b and Supplementary Table 1; Methods). Screens were performed for eight population doublings and enrichment/depletion of single guide (sg)RNAs was assessed by deep sequencing of integrated cassettes from input (t_0) and final (t_8) genomic DNA (Fig. 1b). As expected, gene scores ((GSs) median $\log_2$ fold change in sgRNA abundance between t_8 and t_0) demonstrated temporal genotype-independent depletion and enrichment of sgRNAs targeting essential and tumor-suppressor genes, respectively (Extended Data Fig. 1c and Supplementary Table 2).

[1]Koch Institute for Integrative Cancer Research, Cambridge, MA, USA. [2]Massachusetts Institute of Technology Department of Biology, Cambridge, MA, USA. [3]Howard Hughes Medical Institute, Chevy Chase, MD, USA. [4]Whitehead Institute, Massachusetts Institute of Technology, Cambridge, MA, USA. [5]Massachusetts General Hospital Cancer Center, Boston, MA, USA. [6]Dana-Farber Cancer Institute, Boston, MA, USA. [7]Tufts University, Boston, MA, USA. [8]Harvard Medical School, Boston, MA, USA. [9]Present address: Department of Cancer Biology and Genetics, Memorial Sloan Kettering Cancer Center, New York, NY, USA. [10]Present address: Ben May Department for Cancer Research, University of Chicago, Chicago, IL, USA. [11]These authors contributed equally: Rodrigo Romero, Francisco J. Sánchez-Rivera. ✉e-mail: tjacks@mit.edu

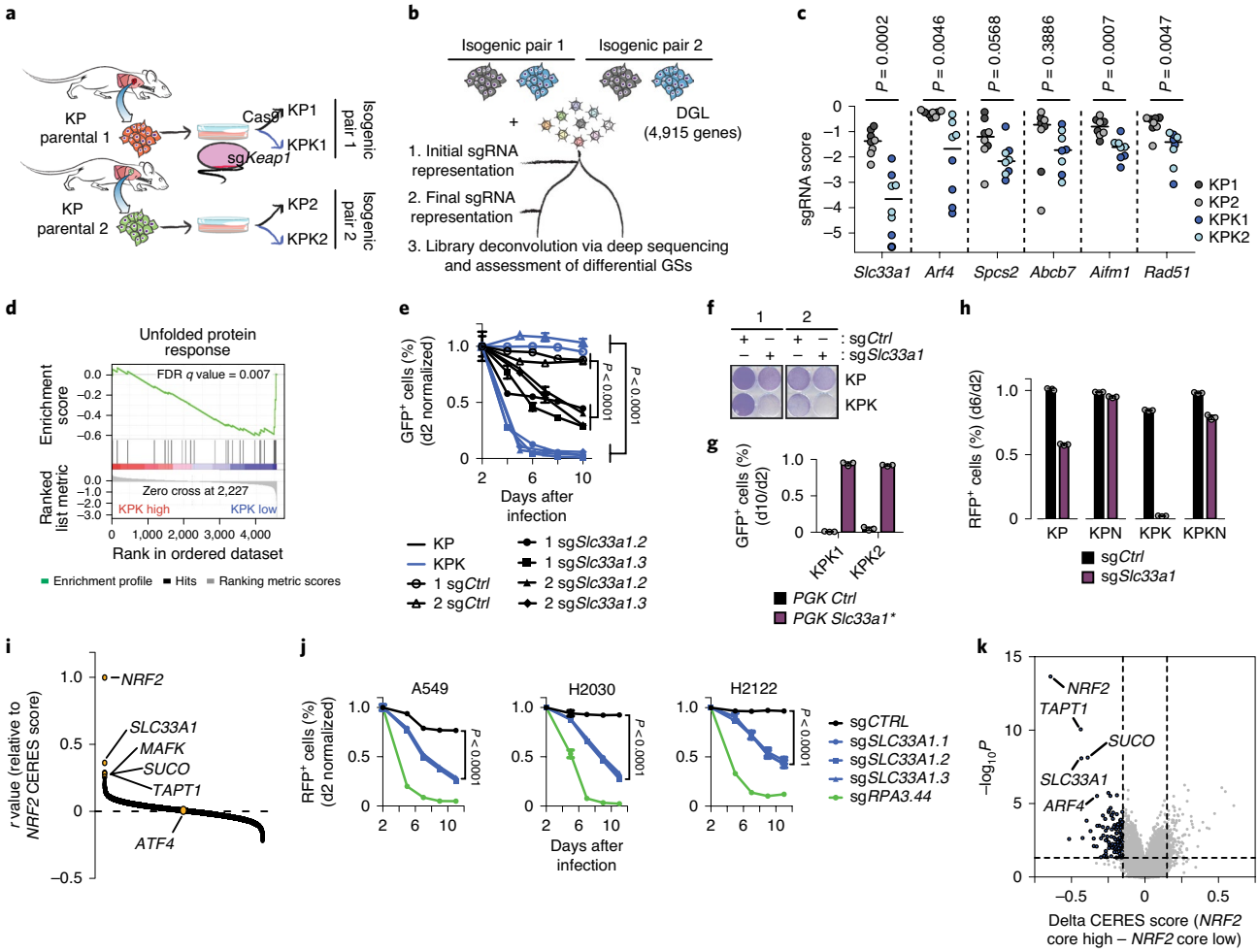

Fig. 1 | A genetic screen for *Keap1*-mutant genetic vulnerabilities uncovers *Slc33a1* as a robust genotype-specific dependency. a, Schematic of the generation of isogenic cell-line pairs. Parental KP cell lines were derived from two individual KP tumor-bearing mice. Parental lines were transfected in vitro with plasmid coexpressing sg*Keap1* and Cas9 and single-cell sorted. Clones were validated for deficiency (KPK) or maintenance (KP) of *Keap1*. **b**, CRISPR-based screening strategy to identify *Keap1*-mutant-specific genetic vulnerabilities. Two isogenic KP and KPK cell-line pairs were infected with the DGL. Genomic DNA was collected at zero (t_0) and eight population doublings (t_8). **c**, Top common differentially depleted genes between each isogenic pair. Each dot represents the $\log_2$ fold change of each sgRNA (sgRNA score) targeting the indicated gene. Bar represents median GS across all sgRNAs targeting the indicated gene per genotype. This experiment was performed once with $n = 8$ biologically independent samples obtained from two independent KP and KPK cell lines that were tested with four independent sgRNAs per gene. *P* values were determined by unpaired two-tailed Student's *t*-test. **d**, GSEA of rank-ordered differential gene scores across the entire DGL screening data from isogenic pair 1 ($n = 2$ cell lines). **e**, Fluorescence competition assays on cells transduced with sg*Ctrl*- or sg*Slc33a1*-expressing pUSPmNG lentiviruses. Plot displays comparison of day 2 (d2) normalized percentage green fluorescent protein (GFP)$^+$ values over time from sg*Ctrl* or sg*Slc33a1* KP and KPK isogenic cell lines. Statistics were derived from the comparison of the average KP-sg*Ctrl* or KPK-sg*Ctrl* values versus the average KP-sg*Slc33a1* or KPK-sg*Slc33a1* values across all *Slc33a1* targeting sgRNAs. This experiment was performed once with $n = 4$ biologically independent samples obtained from two independent KP and KPK cell lines that were tested with two independent sgRNAs. *P* values were determined using two-way analysis of variance (ANOVA) with Tukey's post hoc multiple comparisons test. **f**, Colony formation of KP and KPK isogenic cells targeted with sg*Ctrl* or sg*Slc33a1* (pUSEPR). Data are from $n = 3$ independent culture wells across two independent KP and KPK cell lines targeted with a single sgRNA. **g**, Overexpression of an sgRNA-insensitive *Slc33a1* cDNA (*) or control cDNA (*mScarlet*) in two independent KPK cell lines. Plot displays day 2 normalized percentage GFP$^+$ values from cells 10 d after infection. Data are from $n = 3$ independent culture wells per cell line per expression construct. **h**, Fluorescence competition assays of KP, KP-*Nrf2* KO (KPN), KPK and KPK-*Nrf2* KO (KPKN) isogenic pairs. Plot displays day 2 normalized percentage red fluorescent protein (RFP)$^+$ (pUSEPR) values from sg*Ctrl*- or sg*Slc33a1*-expressing cells 6 d (d6) after infection. Data are from $n = 3$ independent culture wells per cell line per sgRNA. **i**, Waterfall plot of the rank-ordered Pearson correlation coefficient between *NRF2* CERES scores versus all genes screened from the DepMap database v.19Q2 ($n = 563$ cell lines). **j**, Fluorescence competition assay on a panel of *KEAP1*-mutant human LUAD cell lines. Plot displays day 2 normalized percentage RFP$^+$ (pUSEPR) cells marking sg*CTRL*-, sg*SLC33A1*- or sg*RPA3*-infected cells. Statistics were derived from comparison of sg*CTRL* values versus average sg*SLC33A1* values across all *SLC33A1*-targeting sgRNAs. This experiment was performed once with $n = 3$ biologically independent *KEAP1*-mutant human cancer cell lines targeted with three independent sgRNAs. *P* values were determined using two-way ANOVA with Tukey's post hoc multiple comparisons test. **k**, Differential CERES scores between NRF2 core gene set high-ranking cell lines ($n = 42$) versus low-ranking cell lines ($n = 32$) from the DepMap database 19Q2. Horizontal dotted line represents *P* value significance cutoff of $P < 0.05$. Each dot represents the differential CERES score per gene. Blue dots represent genes that pass set threshold values. *P* values were determined by unpaired two-tailed Student's *t*-test. All experiments denoted above are representative of $n = 3$ parallel infections unless otherwise stated. All error bars depicted represent mean ± s.d. Data from a single experiment are shown in **f**–**h** are representative of two independent experiments with similar results. Data for experiments **e**,**g**,**h**, and **j** are available as source data (Source Data Extended Data Fig. 1).

To identify *Keap1*-mutant-specific vulnerabilities, we calculated differential GSs by subtracting KP GSs from KPK GSs, nominating 53 genes in isogenic pair 1 (KPK1-KP1) and 25 in pair 2 (KPK2-KP2) as significantly differentially depleted (false discovery rate (FDR) = 0.05; Methods; Extended Data Fig. 1d,e). *Slc33a1*, *Arf4*, *Spcs2*, *Abcb7*, *Aifm1* and *Rad51* reached significance in both pairs (Fig. 1c, Extended Data Fig. 1d,e and Supplementary Table 2). Notably, SLC33A1, ARF4 and SPCS2 reside in the ER or Golgi[22,23] and ER stress can modulate RAD51 levels and sensitivity to DNA damage[24,25]. In agreement, gene set enrichment analysis (GSEA) of ranked differential GSs identified significant enrichment of ER stress and unfolded protein response (UPR) gene sets (FDR = 0.0073; Fig. 1d and Supplementary Table 3).

Reliance of *Keap1*-mutant cells on *Slc33a1* is NRF2-dependent. To validate differentially depleted genes, we examined the two top-scoring sgRNAs targeting *Slc33a1* and *Arf4* in fluorescence competition and colony-formation assays (Extended Data Fig. 2a,b). We observed clone-specific depletion of sg*Arf4*-targeted KPK1 but not sg*Arf4*-targeted KPK2 cells and thus deprioritized *Arf4* for further evaluation (Extended Data Fig. 2c). Conversely, sg*Slc33a1*-targeted KPK1 and KPK2 cells exhibited robust decreases in growth and while modest growth defects were observed in sg*Slc33a1*-targeted KP cells, the magnitude and kinetics of the effect was significantly less pronounced than in KPK cells ($P < 0.0001$; Fig. 1e,f and Extended Data Fig. 2d). We observed similar decreases in colony formation using inducible short hairpin (sh)RNAs or CRISPR-interference ((CRISPRi) Extended Data Fig. 2e–k). Transduction with sgRNA-resistant *Slc33a1* complementary DNAs rescued gene expression and growth defects in KPK cells targeted with *Slc33a1* sgRNAs, demonstrating on-target dependency (Fig. 1g and Extended Data Fig. 3a). Inactivation of *Nrf2* rescued growth defects caused by *Slc33a1* mutation in KPK cells, indicating that *Slc33a1* dependency is due to NRF2 hyperactivity instead of other KEAP1 clients[6,26] (Fig. 1h and Extended Data Fig. 3b–f). Collectively, these results validate our CRISPR screen and highlight *Slc33a1* as a robust dependency in NRF2-hyperactive *Keap1*-mutant cancer cells.

***KEAP1*-mutant human cancer cells depend on ER-resident genes *SLC33A1*, *SUCO* and *TAPT1*.** We analyzed whole-genome CRISPR screening results from DepMap, which encompasses 563 human cancer cell lines spanning 29 cell lineages[27] (Methods). *SLC33A1*, on average, did not score as a core-essential gene across most human cell lines in DepMap (Extended Data Fig. 3g). However, average *SLC33A1* CERES normalized GSs (hereafter, CERES scores) were ~3.5-fold lower in *KEAP1*/*NRF2*-mutant cancer cell lines ($n = 63$) compared to wild type ($n = 500$; Extended Data Fig. 3h and Supplementary Table 4).

To extend our analyses beyond the DGL, we mined Cancer Coessentiality Networks meta-analyses of depletion screens across different cell types[28]. We identified *NRF2*, *SLC33A1*, *SUCO*, *TAPT1*, *DNAJB11* and *ADPGK* in a single coessential gene cluster using the DepMap dataset as input (Extended Data Fig. 3i). Analogously to top hits identified with the DGL, this cluster is composed entirely of endomembrane-associated genes. To support these analyses further, we calculated Pearson correlation coefficients between *NRF2* CERES scores and the scores of all other genes as an alternative approach to identify genes correlating with *NRF2* dependency (Methods). Remarkably, *SLC33A1* scores had the second highest correlation to *NRF2* scores ($r = 0.361$), followed by *MAFK* ($r = 0.287$), a known NRF2 transcriptional co-activator[29] (Fig. 1i and Extended Data Fig. 3j). Moreover, ER-resident proteins *SUCO* and *TAPT1* (mammalian orthologs of SLP1:EMP65 yeast complex[30]) strongly correlated with *NRF2* dependency (Extended Data Fig. 3g,h and Supplementary Table 4; $r = 0.283$ and $r = 0.258$, respectively). Notably, *SLC33A1* dependency weakly correlated with activating transcription factor 4 (*ATF4*) dependency ($r = -0.001$), a downstream target of the UPR known to exhibit cross-talk with the NRF2 pathway[16] (Fig. 1i, Extended Data Fig. 3k and Supplementary Table 4).

To validate these associations, we confirmed the genotype-specific dependency of human *KEAP1*-mutant cells to *SLC33A1* using fluorescence competition assays (Fig. 1j). To test other dependencies within the *NRF2*-*SLC33A1* coessentiality network, we targeted *Suco* or *Tapt1* in murine KP and KPK cells, which led to decreased fitness only in KPK cells (Extended Data Fig. 3l,m). These data demonstrate that NRF2-hyperactivated cancer cells depend on the function of endomembrane-associated proteins and corroborate the significant depletion of UPR target genes in the DGL (Fig. 1c,d and Extended Data Fig. 3i).

High NRF2 transcriptional signatures correlate with *SLC33A1* dependency. Tumor cells may upregulate NRF2 responses in the absence of *KEAP1*/*NRF2* mutation or *NRF2* amplification[13]. Therefore, we questioned whether the degree of NRF2 transcriptional activity could predict *SLC33A1* dependency. We used a previously established NRF2 core target gene set (hereafter, NRF2 core) or *KEAP1*-mutant transcriptional signature as indicators of NRF2 activation state[14] to stratify cell lines from DepMap into high- or low-scoring cohorts (NRF2 core high-scoring $n = 42$; low-scoring $n = 32$; *KEAP1*-mutant signature high-scoring $n = 43$; low-scoring $n = 21$; Supplementary Table 5; Methods). Comparative CERES score analysis identified 123 (NRF2 core) and 34 (*KEAP1*-mutant signature) statistically significant depleted genes in the high-scoring group and *NRF2*, *SLC33A1*, *SUCO* and *TAPT1* fell within the top 15 genes using either signature ($P < 0.05$; Fig. 1k, Extended Data Fig. 4a and Supplementary Table 5). Although we could not validate *ARF4* dependency in KPK cell lines, we observed significant depletion of *ARF4* in both high-scoring groups. Moreover, despite enrichment of *NRF2*- or *KEAP1*-mutant cell lines in NRF2 core or *KEAP1*-mutant high-scoring groups ($n = 27$, $P = 2.47 \times 10^{-18}$ or $n = 18$, $P = 5.95 \times 10^{-8}$, respectively; hypergeometric test), a substantial fraction of cells did not harbor either mutation ($n = 15$, 35% and $n = 25$, 58%, respectively), highlighting the importance of functionally classifying tumors by NRF2 transcriptional activity rather than *KEAP1* or *NRF2* mutational status alone. We observed a step-wise decrease in GS for *SLC33A1*, *SUCO* and *TAPT1*, but not *RPA3* or *OR12D2* when grouping cell lines by *KEAP1*/*NRF2* wild-type status ($n = 424$), mutant status ($n = 58$) or NRF2 core high-ranking *KEAP1*/*NRF2* wild-type cell lines ($n = 31$). As expected, we did not observe significant differences in CERES scores between wild-type and NRF2 core low-ranking *KEAP1*/*NRF2* wild-type cell lines ($n = 45$). *KEAP1*/*NRF2* mutation displayed the largest fold change compared to wild-type cells (fold change *SLC33A1* = 2.49, *SUCO* = 1.41, *TAPT1* = 1.59), followed by NRF2 core high-ranking cells (fold change *SLC33A1* = 2.41, *SUCO* = 1.5, *TAPT1* = 1.4), further demonstrating that dependency on *SLC33A1*, *SUCO* and *TAPT1* can be stratified by the magnitude of NRF2 transcriptional output independently of *KEAP1*/*NRF2* mutation status (Extended Data Fig. 5b,c).

Loss of *Slc33a1* results in induction of an unfolded protein response. SLC33A1 is an ER-localized transmembrane protein with reported acetyl-coenzyme A (CoA) transport activity[31] (Fig. 2a). *Slc33a1* inactivation in KPK cells led to intracellular blebbing, consistently with previous reports of *Slc33a1* loss of function phenotypes[31,32] (Fig. 2b). Given its reported ER localization and significant KPK-specific depletion in our screens, we performed whole-transcriptome analysis (RNA-seq) on isogenic pair 1 following sg*Ctrl* (nonessential gene, *Olfr102*) or sg*Slc33a1* targeting to define a transcriptional signature of *Slc33a1* deficiency. Differentially expressed genes resulting from *Slc33a1* loss were

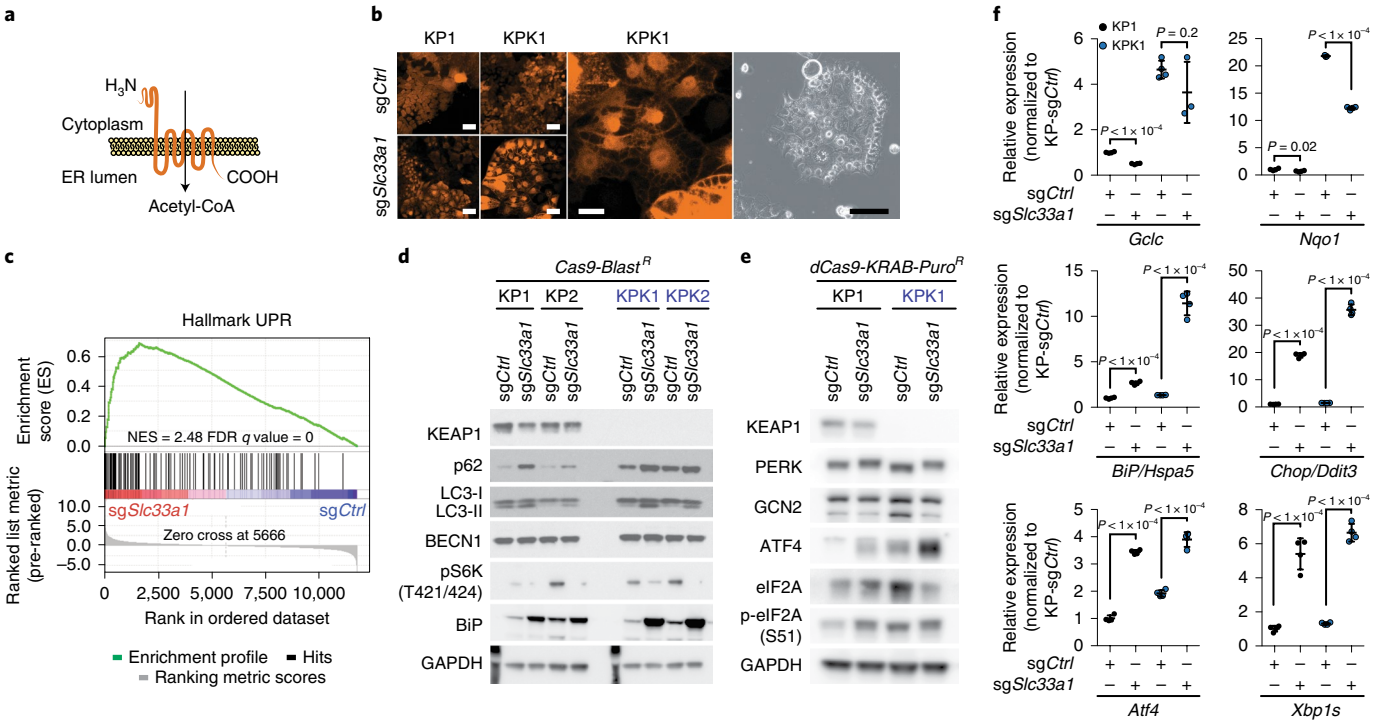

Fig. 2 | Loss of *Slc33a1* promotes the activation of a UPR. a, Schematic of the reported function of SLC33A1. **b**, Confocal images of cytoplasmic-tagRFP (pUSEPR; Methods) labeled isogenic pair 1 infected with sg*Ctrl* or sg*Slc33a1*. Larger picture denotes increased magnification of KPK-sg*Slc33a1* cells (scale bar, 20 μm). Phase contrast microscopy of KPK-*Slc33a1* cells (far right). Data are representative of $n = 3$ independent experiments with similar results. All scale bars denote 100 μm unless otherwise stated. **c**, GSEA enrichment plot of the Hallmark UPR signature enriched in sg*Slc33a1*-targeted cells compared to sg*Ctrl*-targeted KP1 or KPK1 cell lines. **d**, Western blot analysis of Cas9-expressing KP and KPK isogenic pairs targeted with sg*Ctrl* or sg*Slc33a1* for autophagy and UPR markers. GAPDH, glyceraldehyde 3-phosphate dehydrogenase. **e**, Western blot analysis of dCas9-KRAB expressing KP and KPK isogenic pairs targeted with sg*Ctrl* or sg*Slc33a1* for UPR markers. **f**, Quantitative PCR (qPCR) analysis of UPR or NRF2 target genes in Cas9-expressing isogenic pair 1 targeted with sg*Ctrl* or sg*Slc33a1*. Bars represent messenger RNA expression normalized to *Actb* then to KP-sg*Ctrl* and error bars represent mean ± s.d. from the mean across $n = 3$ or 4 independent experiments. *P* values were determined by unpaired two-tailed Student's *t*-test. Data from a single experiment shown in **d** and **e** are representative of two independent experiments with similar results. Data for experiment **f** and unmodified gel images for **d** and **e** are available as source data (Source Data Figs. 1 and 2 and Source Data Extended Data Figs. 1 and 2).

enriched in the UPR pathway, further supporting a role for *Slc33a1* in maintaining ER homeostasis in NRF2-hyperactivated cells (normalized enrichment score (NES) = 2.48; FDR = 0; Fig. 2c and Supplementary Table 6).

Using previously defined UPR transcriptional signatures[33], we observed significant positive enrichment of gene sets associated with ER chaperones (NES = 2.13; FDR = 0), aminoacyl transfer RNA synthetase (NES = 1.91; FDR = 0), ER/Golgi trafficking (NES = 1.68; FDR = 0.0146) and ER-associated protein degradation ((ERAD) NES = 1.61; FDR = 0.025) in sg*Slc33a1*-targeted cells (Extended Data Fig. 5a–d and Supplementary Table 7). Inactivation of *Slc33a1* increased p62 and LC3-II expression, PERK mobility shift and an increased ratio of phospho-to-total eIF2A in KPK cells, with no change in GCN2 levels, all consistent with induction of autophagy and a UPR (Fig. 2d,e). Increased expression of UPR target genes was evident in KP-sg*Slc33a1* and KPK-sg*Slc33a1* cells by both protein (binding immunoglobulin protein (BiP)/HSPA5, ATF4; Fig. 2d,e) and gene expression analysis (*BiP*/*Hspa5*, *Chop*/*Ddit3*, *Atf4* and *Xbp1*s; Fig. 2f). Notably, the level of induction of *Atf4*, *BiP* and *Chop*/*Ddit3* was greater in KPK-sg*Slc33a1* compared to KP-sg*Slc33a1* cells, suggesting that *Keap1* loss results in enhanced induction of an UPR in the face of this form of ER stress (Fig. 2d–f).

***Slc33a1* dependency is rescued by inhibition of glutathione synthesis.** KPK cells upregulate the NRF2 pathway, resulting in increased GSH synthesis[14] likely due to upregulation of NRF2-dependent enzymes directly involved in GSH synthesis (glutamate cysteine ligase catalytic (GCLC) subunit; *Gclc*)[34] or uptake of L-cystine that is necessary for GSH synthesis (system xCT encoded by *Slc7a11* and *Slc3a2*; Fig. 3a). Yeast studies have demonstrated that enhanced extracellular GSH uptake results in growth inhibition and cell death in a GSH dose-dependent manner[35]. We hypothesized that concomitant increase in NRF2-dependent GSH synthesis and genetic perturbation of endomembrane-associated genes might induce an UPR, which may explain the increased dependency of *Keap1*-mutant cells on *Slc33a1*, *Suco* and *Tapt1*. To test this hypothesis, we probed the GSH synthesis and recycling pathways using genetic and small-molecule approaches. Pharmacological inhibition of GCLC (L-buthionine sulfoximine (BSO))[36] both reduced total GSH within 48 h of treatment and rescued the fitness defect of sg*Slc33a1*-, sg*Suco*- and sg*Tapt1*-targeted KPK cells (Fig. 3b and Extended Data Fig. 5e,f). Similarly, BSO treatment rescued the effects of shRNA-mediated *Slc33a1* knockdown (Extended Data Fig. 5g) and blunted the enrichment of sg*Gclc* cells over time, further supporting its on-target activity in rescuing viability defects caused by *Slc33a1* loss (Fig. 3c). Notably, BSO treatment also rescued fitness defects of *SLC33A1*-deficient *KEAP1*-mutant human LUAD cells (Fig. 3d). To determine whether additional NRF2-dependent metabolic changes could also modulate *Slc33a1* dependence, we treated cells with the xCT inhibitor erastin[37], *N*-acetyl cysteine (NAC) or dimethyl-2-oxoglutarate ((DMG)

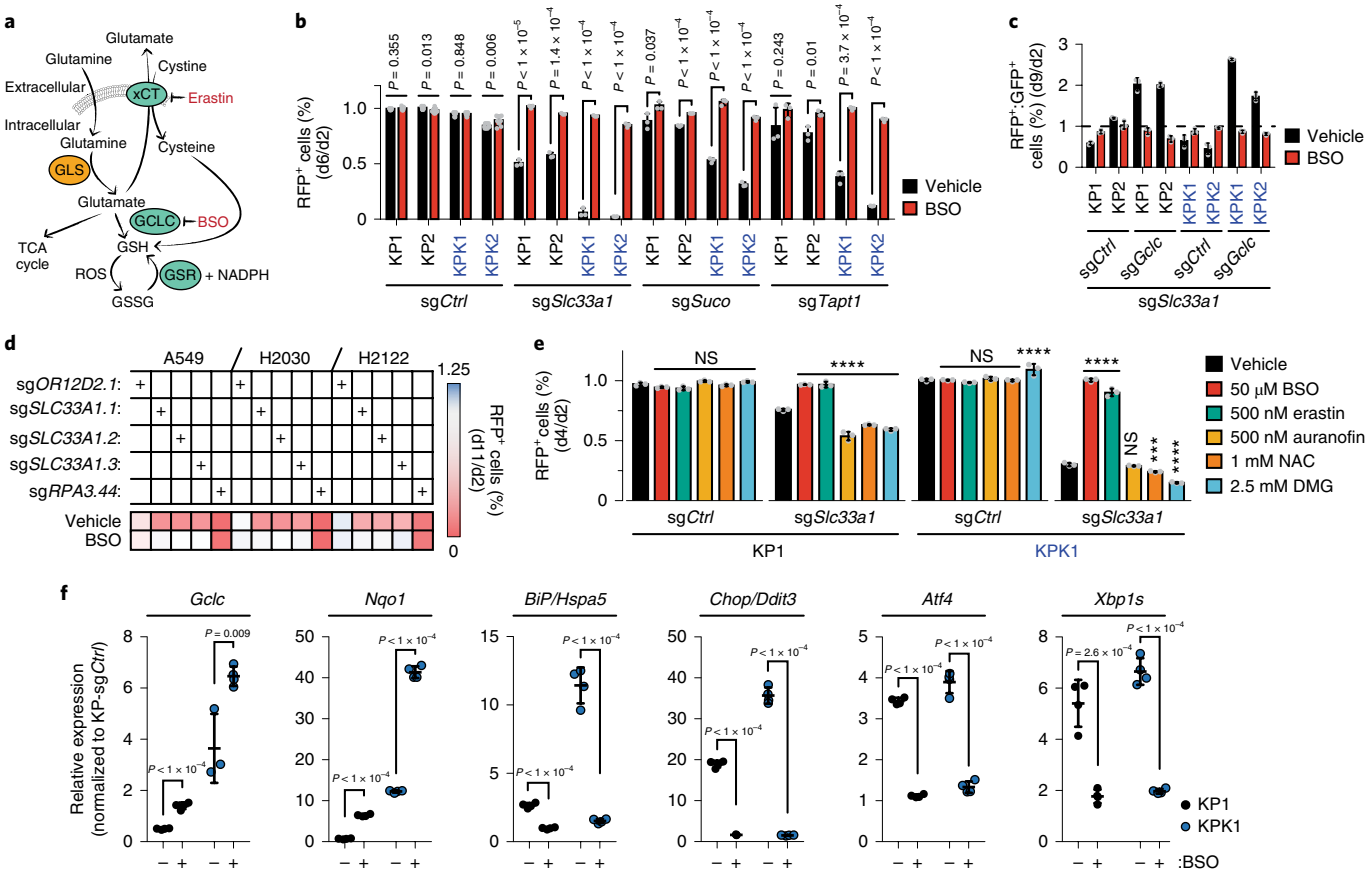

Fig. 3 | Loss of *Slc33a1* is rescued by inhibiting glutathione synthesis. a, Schematic of the biosynthetic pathways contributing to GSH synthesis. Enzymes marked in blue circles are direct NRF2 target genes. Small-molecule inhibitors are in red font. **b**, Fluorescence competition assay in KP and KPK isogenic cell lines infected with pUSEPR-sg*Ctrl*, pUSEPR-sg*Slc33a1*, pUSEPR-sg*Suco* or pUSEPR-sg*Tapt1*. All cell and sgRNA combinations were treated with vehicle or 50 μM BSO. Plots display percentage RFP$^+$ values normalized to day 2 after infection values. Data are representative of $n = 3$ independent experiments across two independent KP or KPK cell lines targeted with the denoted sgRNA. *P* values were determined by unpaired two-tailed Student's *t*-test. **c**, Fluorescence competition assay of RFP$^+$-*Slc33a1*-deficient cells (pUSEPR) reinfected with pUSPmNG-sg*Ctrl* or pUSPmNG-sg*Gclc*. Plots display double positive percentage RFP:GFP values normalized to day 2 percentage RFP:GFP values. Cells were treated as in **b**. Data are from $n = 3$ independent culture wells per cell line per sgRNA. **d**, Heat map of fluorescence competition assays in *KEAP1*-mutant human LUAD cell lines (pUSEPR) treated as in **b**. Data are normalized as in **b** and are from $n = 3$ independent culture wells per *KEAP1*-mutant human cancer cell line. **e**, Fluorescence competition assay of cells transduced with pUSEPR-sg*Ctrl* or pUSEPR-sg*Slc33a1*. Plots display percentage RFP normalized to day 2 post-infection values. Cells were treated with vehicle, 50 μM BSO, 500 nM erastin, 500 nM auranofin, 1 mM NAC or 2.5 mM DMG. Data are representative of $n = 3$ independent experiments per treatment condition. *P* values were determined using two-way ANOVA with Dunnett's post hoc multiple comparisons test. $^*P < 0.05$, $^{**}P < 0.01$, $^{***}P < 0.001$, $^{****}P < 0.0001$; NS, not significant. **f**, qPCR validation of UPR or NRF2 target genes in isogenic pair 1 targeted with sg*Ctrl* or sg*Slc33a1*. Cells were treated as in **b**. Bars represent mRNA expression normalized to *Actb* then to KP-sg*Ctrl*, and error bars represent mean ± s.d. from the mean across $n = 3$ or 4 independent experiments per treatment condition. *P* values were determined by unpaired two-tailed Student's *t*-test. Data from a single experiment shown in **c** and **d** are representative of two independent experiments with similar results. Data for experiments **b**–**f** are available as source data (Source Data Extended Data Figs. 1 and 2).

cell-permeable α-ketoglutarate). Similarly to BSO, erastin fully rescued the fitness defect in sg*Slc33a1*-targeted cells (Fig. 3e and Extended Data Fig. 5f) and, notably, neither agent was able to rescue sg*Rpa3*-targeted cells (Extended Data Fig. 5h). NAC and DMG did not rescue the fitness of *Slc33a1*-deficient KPK cells (Fig. 3e). These results suggest that *Slc33a1* dependency cannot be explained by a generic increase in ROS, decreased cysteine availability or changes in central carbon metabolism associated with *Keap1* loss[15], respectively. However, these results do not rule out the possibility that organelle-specific changes occur upon *Slc33a1* loss. Perturbation of the GSH to oxidized GSH (GSSG) ratio to favor GSSG accumulation via menadione-induced NADPH oxidation[38] failed to rescue *Slc33a1*-deficient KPK cells (Extended Data Fig. 5i). Moreover, treatment with the thioredoxin reductase-1 inhibitor, auranofin[39], failed to rescue the effects of *Slc33a1* loss, suggesting that total pools or de novo synthesis of GSH, but not thioredoxin, mediate *Slc33a1* dependence (Fig. 3e). Collectively, these data demonstrate that inhibition of GSH synthesis is sufficient for rescuing the effects of *Slc33a1* loss.

To test whether induction of the UPR is prevented by GSH depletion, we treated KP1-sg*Slc33a1* or KPK1-sg*Slc33a1* and KP1-sg*Ctrl* or KPK1-sg*Ctrl* cells with BSO and quantified relative expression of a panel of UPR target genes. Consistently with recent observations, short-term treatment with BSO did not impact UPR gene induction in sg*Ctrl* cells[40] (Fig. 3f). BSO treatment in KP and KPK cells induced NRF2 pathway targets (*Gclc*, *Nqo1*), consistent with decreases in total GSH pools, leading to an oxidized environment that activates NRF2 signaling (Fig. 3f). Notably, BSO treatment rescued UPR gene induction in sg*Slc33a1* cells, suggesting that high levels of GSH synthesis is a critical mediator of UPR induction

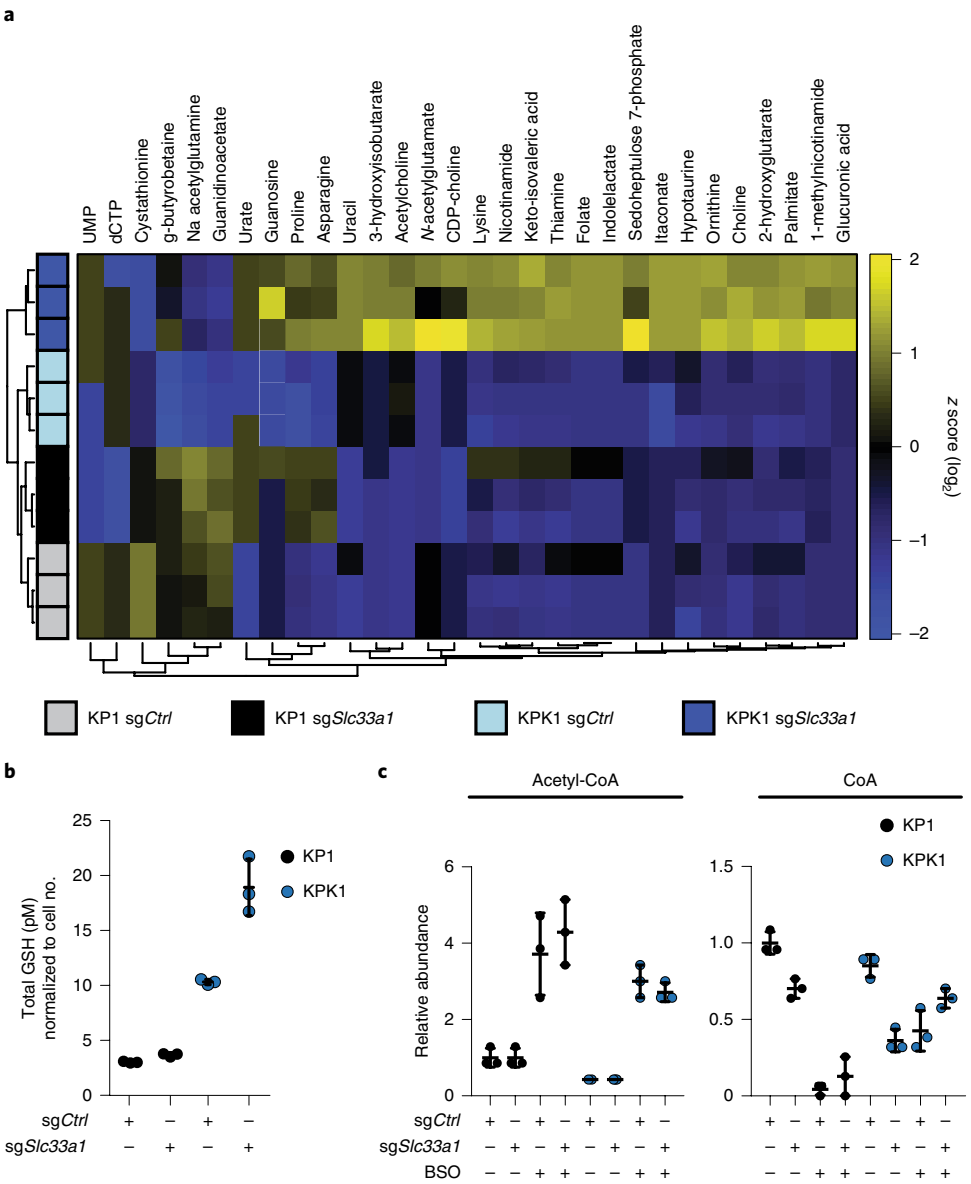

Fig. 4 | *Slc33a1* loss results in metabolic rewiring. a, Unsupervised clustering of significant differentially detectable polar metabolites. Each row represents a different metabolite. Each column represents a different sample. Each cell-line condition was completed in technical triplicates. Data are normalized by cell counts for each cell line. UMP, uridine monophosphate; dCTP, 2′-deoxycytidine-5′-triphosphate; CDP, cytidine (5′)-diphosphocoline. **b**, GSH concentrations of KP and KPK cells 72 h after transduction with the denoted sgRNAs. Data are representative of $n = 3$ independent culture well per cell line per sgRNA. **c**, Acetyl-CoA and CoA relative abundances from data represented in **a**. Cells were treated with or without 50 μM BSO for 48 h. Data are normalized by cell counts for each cell line. Data are representative of $n = 3$ independent culture wells per cell line per sgRNA. All experiments denoted above are representative of $n = 3$ parallel infections. All error bars represent mean ± s.d. Data from a single experiment are shown in **a**–**c**. Data for experiment **b** are available as source data (Source Data Extended Data Fig. 3).

following *Slc33a1* loss (Fig. 3f). To determine whether *Keap1* loss sensitizes cells to ER stress and UPR induction, we treated KP and KPK cells with tunicamycin and thapsigargin, which are commonly used small-molecule inducers of the UPR[32]. On average, KPK cells displayed increased sensitivity to treatment (Extended Data Fig. 6a–c). KP1 and KPK1 cells displayed similar sensitivity to tunicamycin, which we speculate is due to an overall increase in NRF2 pathway activation, as we previously detected increased GCLC protein in this line compared to other KP cell lines[14]. Notably, co-treatment with BSO led to significantly increased thapsigargin resistance, with a larger magnitude of rescue in KPK cells (Extended Data Fig. 6d–f). Together, these data suggest that increased GSH synthesis promoted by *Keap1* mutation leads to heightened sensitivity to genetic perturbations of ER-localized proteins (for example, loss of *Slc33a1*, *Suco* or *Tapt1*) or chemical perturbations (for example, thapsigargin treatment).

Loss of *Slc33a1* is associated with widespread metabolic changes. *Slc33a1* has been reported to transport acetyl-CoA into the ER lumen[41]. Therefore, *Slc33a1* inactivation could disrupt cellular metabolic processes that depend on acetyl-CoA transport. To characterize differences in polar metabolite levels and usage following *Slc33a1* loss, we performed liquid chromatography–mass spectrometry (LC–MS) in KP-sg*Ctrl* and KPK-sg*Ctrl* or -sg*Slc33a1* cells maintained in BSO for 48 h or after withdrawal of BSO for 48 h (a time point at which there is no significant cell death; Supplementary Table 8).

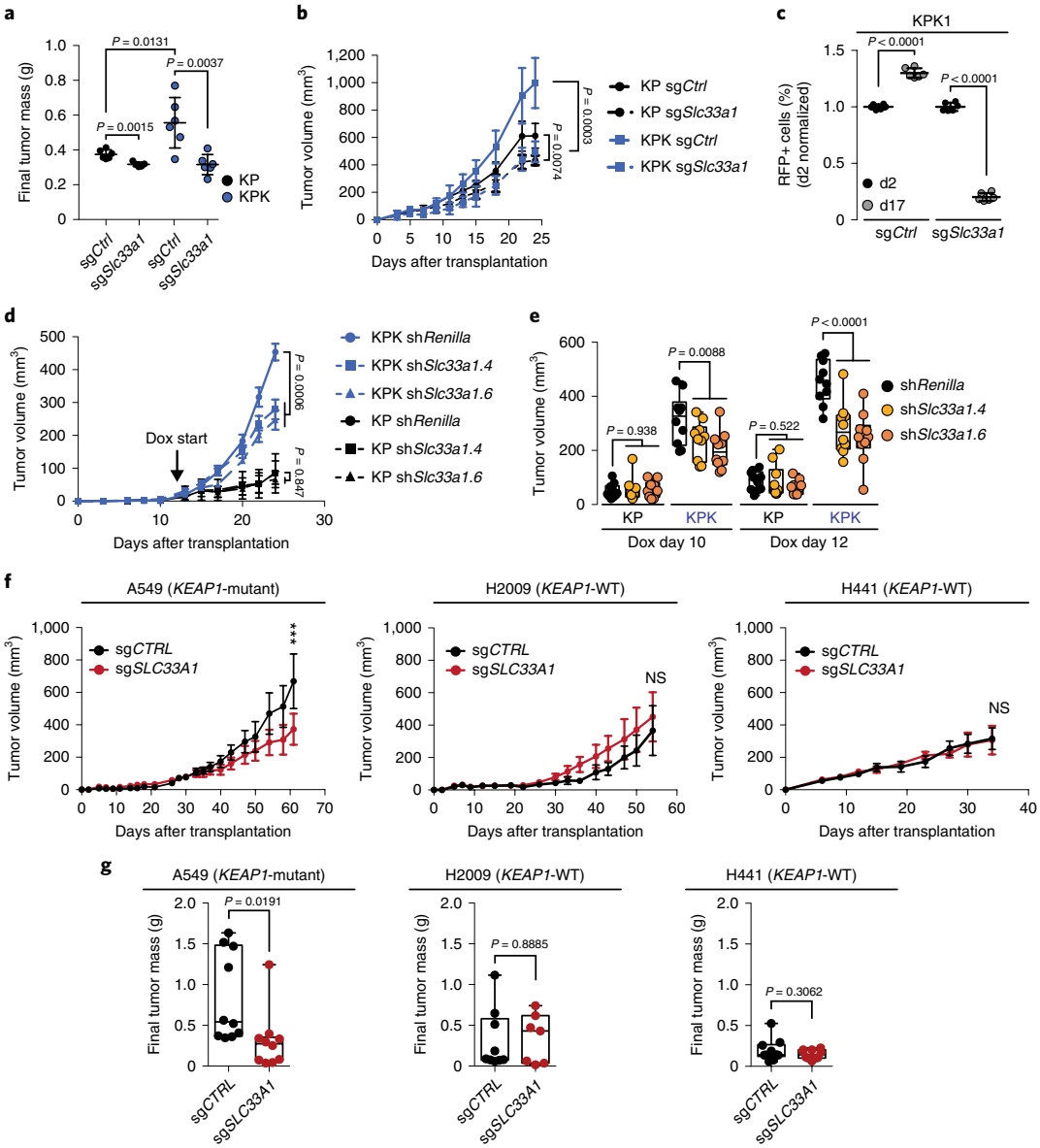

Fig. 5 | *Slc33a1* loss validates as a *Keap1*-mutant-specific vulnerability in transplant models. a, Final subcutaneous tumor masses obtained from transplantation of indicated cell lines into immunocompromised mice. Data are representative of $n=5$ or 6 tumors from three total mice per group. Error bars represent mean ± s.d. *P* values were determined by unpaired two-tailed Student's *t*-test. **b**, Subcutaneous tumor volumes of KP and KPK cells transduced with the indicated sgRNAs injected into immunocompromised mice. Data are representative of $n=5$ or 6 tumors from three total mice per group. Error bars represent mean ± s.e.m. *P* values were determined using two-way ANOVA with Sidak's post hoc multiple comparisons test. **c**, In vivo fluorescence-based competition assay of GFP-labeled KPK1 cells injected into immunocompromised mice. KPK1 cells were transduced with pUSEPR constructs containing the indicated sgRNAs. Transduced cell representation was normalized to the percentage of RFP$^+$ cells at d2 (preimplantation). Data are representative of $n=6$ tumors from three total mice per group. Error bars represent mean ± s.d. *P* values were determined by paired two-tailed Student's *t*-test. **d**, Subcutaneous tumor volumes of KP or KPK cells transduced with doxycycline (dox)-inducible shRNAs targeting *Renilla* or *Slc33a1* (LVt-TSTOP; see Methods). Arrow indicates timepoint at which mice began doxycycline treatment. Error bars represent mean ± s.e.m. Data from $n=10$ tumors were derived from five mice per group. *P* values were determined using two-way ANOVA with Dunnet's post hoc multiple comparisons test. **e**, Tumor volumes were related to **d** at the indicated time points. Statistics were determined by comparison of the sh*Renilla* group versus both sh*Slc33a1* groups per genotype per time point. Data from $n=10$ tumors were derived from five mice per group. *P* values were determined using one-way ANOVA with Dunnet's post hoc multiple comparisons test. **f**, Xenografts of *KEAP1*-mutant A549 or *KEAP1*-wild-type H2009 and H441 human lung cancer cell lines infected with either sg*CTRL* or sg*SLC33A1* (pUSEPR). Error bars denote mean ± s.e.m. A549, $n=10$ sg*CTRL* or $n=10$ sg*SLC33A1* xenografts; H2009, $n=9$ sg*CTRL* xenografts or $n=10$ sg*SLC33A1* xenografts; H441, $n=10$ sg*CTRL* xenografts or $n=10$ sg*SLC33A1* xenografts from five mice per cell line per group. *P* values were determined using two-way ANOVA with Sidak's post hoc multiple comparisons test for each cell line sg*CTRL*:sg*SLC33A1* pair. $^*P<0.05$, $^{**}P<0.01$, $^{***}P<0.001$, $^{****}P<0.0001$. **g**, Final subcutaneous tumor masses obtained from xenografts of indicated cell lines into immunocompromised mice. A549, $n=10$ sg*CTRL* xenografts or $n=10$ sg*SLC33A1* xenografts from five total mice per group. H2009, $n=9$ sg*CTRL* xenografts from five total mice per group or $n=7$ sg*SLC33A1* xenografts from four total mice per group. H441, $n=10$ sg*CTRL* xenografts or $n=10$ sg*SLC33A1* xenografts from five total mice per group. *P* values were determined by unpaired two-tailed Student's *t*-test. All error bars depicted represent mean ± s.d. unless otherwise noted. Horizontal lines in box plots represent 10th, 25th, 50th (median), 75th and 90th (percentiles). Data for experiments **a**–**g** are available as source data (Source Data Extended Data Fig. 4).

Steady-state levels of 45 of 167 detected metabolites were significantly different across all samples (Supplementary Table 8). Unsupervised hierarchical clustering revealed three major clusters, with all technical replicates of vehicle-treated KPK-sg*Slc33a1* cells clustering separately from the rest (Fig. 4a). Consistently with earlier reports, we detected reduced tricarboxylic acid (TCA) cycle intermediates in KPK-sg*Ctrl* compared to KP-sg*Ctrl* cells, increased intracellular GSH and concomitant decreases in intracellular α-ketoglutarate[14,15] (Extended Data Fig. 7a,b). Notably, TCA-derived metabolites were significantly increased in KPK cells targeted with sg*Slc33a1*, consistent with *Slc33a1* loss either boosting TCA cycle utilization or causing increases in TCA cycle components via autophagy-mediated breakdown[42] (Extended Data Fig. 7a). In addition to increased total levels of GSH (Fig. 4b), we observed increased GSSG levels, resulting in decreased GSH:GSSG ratios in KPK-sg*Slc33a1* cells compared to KPK-sg*Ctrl* cells (Extended Data Fig. 7b).

To determine whether changes in intracellular metabolites arise from changes in influx or secretion, we used gas chromatography–mass spectrometry (GC–MS) to assess changes in metabolite consumption or secretion in tissue culture medium. This confirmed an increase in glutamine and cystine consumption and an increase in glutamate secretion in KPK-sg*Ctrl* cells, likely associated with increased demand for GSH synthesis, resulting from *Keap1* mutation (Extended Data Fig. 7c and Supplementary Table 9). The increase in glutamine and cystine consumption, as well as glutamate secretion, was exacerbated upon *Slc33a1* loss (Extended Data Fig. 7c).

Given that *Slc33a1* is reported to be involved in cytoplasmic-to-ER acetyl-CoA transport[31,42] and that steady-state acetyl-CoA and CoA pools were lower in KPK-sg*Ctrl* cells relative to KP-sg*Ctrl* cells (Fig. 4c and Extended Data Fig. 7a), it is possible that KPK cells were more sensitive to *Slc33a1* loss due to limitations in transporting acetyl-CoA (and other undefined metabolites) into the ER. Moreover, we detected further decreases of intracellular CoA and trans-sulfuration intermediates in KPK-sg*Slc33a1* cells relative to KPK-sg*Ctrl* cells (Supplementary Table 8). A potential explanation for this observation is that GSH or GSH synthesis may directly impact the availability of intracellular acetyl-CoA. Supporting this, BSO-treated KPK-sg*Slc33a1* cells clustered most closely with KP-sg*Ctrl* and KPK-sg*Ctrl* cells and displayed an increased relative abundance of acetyl-CoA and CoA (Fig. 4c and Extended Data Fig. 7d,e). Altogether, these data demonstrate that *Slc33a1* loss results in metabolite changes in murine *Kras*-mutant LUAD cell lines, particularly in combination with *Keap1* loss. However, whether acetyl-CoA is the relevant metabolite that explains *Slc33a1* dependency remains to be determined.

Transplant models and GEMMs of *Keap1*-mutant LUAD are dependent on *Slc33a1*. To address the impact of *Slc33a1* loss in vivo, we first transplanted KP1 or KPK1 cell lines expressing sg*Ctrl* or sg*Slc33a1* into the flanks of immunocompromised mice and measured longitudinal growth, final subcutaneous tumor mass and in vivo competitive fitness, confirming a dependency for *Slc33a1* in transplanted KPK tumors (Fig. 5a–c). Moreover, inducible shRNA-mediated knockdown (Extended Data Fig. 2e–h) of *Slc33a1* after tumor initiation led to a significant decrease in tumor volume in KPK but not KP transplants compared to sh*Renilla* controls ($P=0.0006$; Fig. 5d,e). Additionally, sg*SLC33A1*-targeted A549 xenografts (*KEAP1*-mutant) grew more slowly (A549: $P<0.001$) and generated smaller tumors (A549: fold change = 2.711, $P=0.019$) compared to sg*CTRL*-targeted tumors (Fig. 5f,g). Notably, we did not observe decreases in tumor size in *KEAP1*-wild-type sg*SLC33A1*-targeted H2009 or H441 xenografts (Fig. 5f,g). These data confirmed *Slc33a1* as a dependency of *Keap1*-mutant tumors and prompted us to perform further validation in a GEMM of LUAD[43] that recapitulates the differential nutrient availability between tumors and surrounding normal tissues, as well as the native lung microenvironment[44,45]. We utilized the $Kras^{LSL\text{-}G12D/+}$ (where LSL is *loxP-STOP-loxP*);$p53^{fl/fl}$ GEMM of LUAD (hereafter, KP)[46,47], in which tumors are induced upon intratracheal instillation of lentivirus expressing Cre recombinase[43,48]. KP mice were crossed to conditional strains of *Keap1* (ref. [49]) and *Cas9* ($Rosa26^{LSL\text{-}Cas9}$; ref. [50]) for NRF2 pathway activation and somatic editing of genes within initiated lung tumors, respectively, generating $Kras^{LSL\text{-}G12D/+}$;$p53^{fl/fl}$;$Keap1^{fl/fl}$;$Rosa26^{LSL\text{-}Cas9/+}$ mice (hereafter, KPC or KPKC). To assess the effects of *Slc33a1* targeting in *Keap1*-wild-type and *Keap1*-null tumors, we induced tumors in KPC or KPKC mice with pUSEC (U6-sgRNA-H1-sgRNA-EFS-Cre) lentivirus expressing Cre recombinase and tandem sgRNAs targeting *Slc33a1* or *Olfr102* (sg*Ctrl*; Fig. 6a and Extended Data Fig. 8a; Methods).

Histological analysis revealed an increase in high-grade adenocarcinomas, tumor burden, tumor number and proportion of proliferating cells in KPKC-sg*Ctrl* mice compared to KPC-sg*Ctrl* mice (Fig. 6b–e), consistent with previous studies[14]. We did not detect significant differences in grade, tumor burden or tumor number in KPC-sg*Slc33a1* compared to KPC-sg*Ctrl* mice (Fig. 6b–d). However, there was a significant reduction in high-grade adenocarcinomas (grade 2 fold change = 6.6, $P=8.18\times10^{-9}$; grade 3 fold change = 4.7, $P=2.81\times10^{-6}$; grade 4 fold change = 23, $P=0.025$), tumor burden (fold change = 4.36, $P=5.95\times10^{-7}$) and number (fold change = 2.06, $P=0.0147$) in KPKC-sg*Slc33a1* versus KPKC-sg*Ctrl* mice (Fig. 6b–d). We did not detect significant differences in the mitotic index of KPKC-sg*Slc33a1* tumors compared to KPKC-sg*Ctrl* tumors (Fig. 6e and Extended Data Fig. 8b), suggesting that the reduced tumor burden of KPKC-sg*Slc33a1* mice is likely due to decreased tumor initiation and/or a heightened barrier for transition to higher grade LUAD (Fig. 6e).

We hypothesized that early lesions may have been enriched for incomplete *Keap1* recombination (resulting in decreased NRF2 activation) or incomplete deletion of *Slc33a1*. Supporting this hypothesis, deep sequencing of the *Slc33a1* locus in microdissected tumors from sg*Slc33a1*-targeted mice revealed a significantly greater ratio of wild-type sequence reads and nonframeshift mutations (which may preserve gene function) in KPKC tumors compared to KPC tumors, indicating strong selection against combined deletion of *Keap1* and *Slc33a1* ($P=0.0102$, Fig. 6f,g and Extended Data Fig. 8c–e). Furthermore, while *Keap1* recombined tumors displayed enhanced expression of the NRF2 target gene, NQO1 (refs. [13,14]; Fig. 6h), we observed a nonsignificant trend toward decreased NQO1 positive tumors in KPKC-sg*Slc33a1* animals (Extended Data Fig. 8f). These results suggest that tumors may escape via failure to completely recombine *Keap1* or alternative mechanisms to dampen the NRF2 program. Collectively, these data validate *Slc33a1* as a robust dependency in *Keap1*-mutant LUAD in vivo and *Keap1*-wild-type tumors that have upregulated the NRF2 pathway via other genetic or epigenetic mechanisms may also show sensitivity to *Slc33a1* loss or inhibition.

Whole-genome CRISPR screen identifies suppressors of *Slc33a1* dependency. To gain further insights into the biology of *Slc33a1*, *Suco* and *Tapt1* in a *Keap1*-mutant context, as well as identify patient genotypes that may not respond to SLC33A1 inhibition, we performed an unbiased whole-genome CRISPR screen using a previously established library[51] (hereafter, Brie; Fig. 7a). To that end, we leveraged BSO-mediated rescue to isolate KPK-*Slc33a1*, KPK-*Suco* and KPK-*Tapt1* knockout clones (Fig. 7a and Extended Data Fig. 9a,b). Four KPK-*Slc33a1* single-cell clones were pooled, transduced with the Brie library and separated into BSO- or vehicle-treated conditions. Library representation was determined by deep sequencing of sgRNAs amplified from BSO or vehicle-treated cells at early (t_0) and eight population doublings post-transduction (t_8; Fig. 7b, Extended Data Fig. 9c and Supplementary Table 10). Median GS analysis within vehicle-treated groups identified *Nrf2*, *Gclc* and *Gclm* as the top enriched genes, validating our previous data using

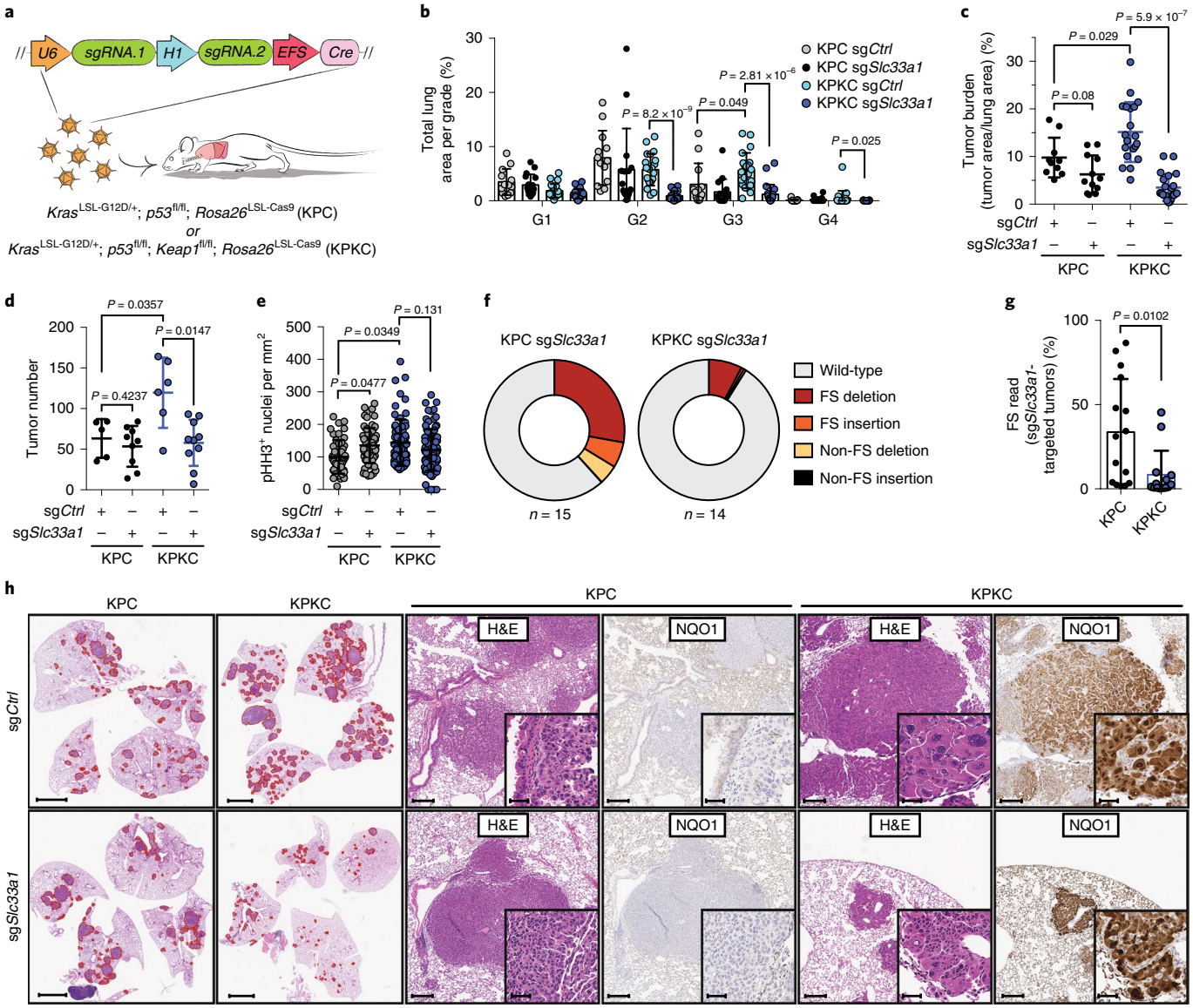

Fig. 6 | *Keap1*-mutant tumors harbor an increased dependency for *Slc33a1* in an autochthonous model of murine lung adenocarcinoma. a, Schematic representation of KPC or KPKC mice intratracheally infected with pUSEC lentiviruses containing dual sgRNAs targeting *Slc33a1* or *Olfr102* (sg*Ctrl*). **b**, Distribution of histological tumor grades (G1–G4) in KPC or KPKC mice 20 weeks after infection with pUSEC lentiviruses expressing control (sg*Ctrl*, KPC, $n=10$ mice; KPKC, $n=20$ mice) or sg*Slc33a1* (KPC, $n=12$ mice; KPKC, $n=22$ mice). *P* values were determined using two-sided Mann–Whitney *U*-test with Holm's multiple comparisons correction. **c**, Combined quantification of tumor burden in KPC or KPKC mice after infection with pUSEC lentiviruses. Mouse numbers are equivalent to **b**. Error bars denote mean ± s.e.m. *P* values were determined using two-sided Mann–Whitney *U*-test with Holm's multiple comparisons correction. **d**, Combined quantification of average tumor number in KPC or KPKC mice after infection with pUSEC lentiviruses. Mouse numbers equivalent to **b**. *P* values were determined using two-sided Mann–Whitney *U*-test with Holm's multiple comparisons correction. **e**, Quantification of phosphorylated histone H3 $(pHH3)^+$ nuclei per squared millimeter of tumor for assessment of the mitotic index of tumor cells from lung tumors in KPC or KPKC mice at 20 weeks after infection with the indicated pUSEC lentivirus. Mouse numbers are equivalent to **b**. Fifty tumors were blindly selected and the average number of $pHH3^+$ nuclei were averaged per mouse followed by averaging across mice per group. *P* values were determined using two-sided Mann–Whitney *U*-test with Holm's multiple comparisons correction. **f**, Fraction of mutant and wild-type reads within individually plucked tumors from 20-week pUSEC-sg*Slc33a1* lentiviral-infected KPC (mean of $n=15$ tumors from seven mice) and KPKC mice (mean of $n=14$ tumors from seven mice). **g**, Mean number of frameshift (FS) reads from pUSEC-sg*Slc33a1*-infected KPC (mean of $n=15$ tumors from seven mice) and KPKC mice (mean of $n=14$ tumors from seven mice). *P* values were determined by unpaired two-tailed Student's *t*-test. **h**, Representative hematoxylin and eosin (H&E) and immunohistochemistry (IHC) staining of serial sections from lung tumors of KPC or KPKC mice 20 weeks after infection with pUSEC-sg*Ctrl* (top) or pUSEC-sg*Slc33a1* (bottom). First panels show H&E staining of KPC and KPKC tumor sections, which were used for calculating overall lung tumor burden (scale bar, 2 mm). Stains were completed across all mice as in **b** with similar results. Second panels, higher-magnification H&E staining of representative tumors (scale bar, 100 μm; insets depict higher-magnification images, scale bar, 50 μm). Third panels, representative IHC staining for NRF2 target gene, NQO1. This was repeated for KPKC mice. All error bars denote mean ± s.d. unless otherwise stated. Data for experiment **e** are available as source data (Source Data Extended Data Fig. 4).

an unbiased approach (Fig. 7c). Given that *Slc33a1* loss results in a potent growth disadvantage in KPK cells, we hypothesized that any gene at t_8 with a positive sgRNA count across all replicate infections and represented by ≥2 individual sgRNAs would represent true biological hits capable of rescuing KPK-*Slc33a1* deficiency. Using these thresholds (Methods), we identified a number of genes, including

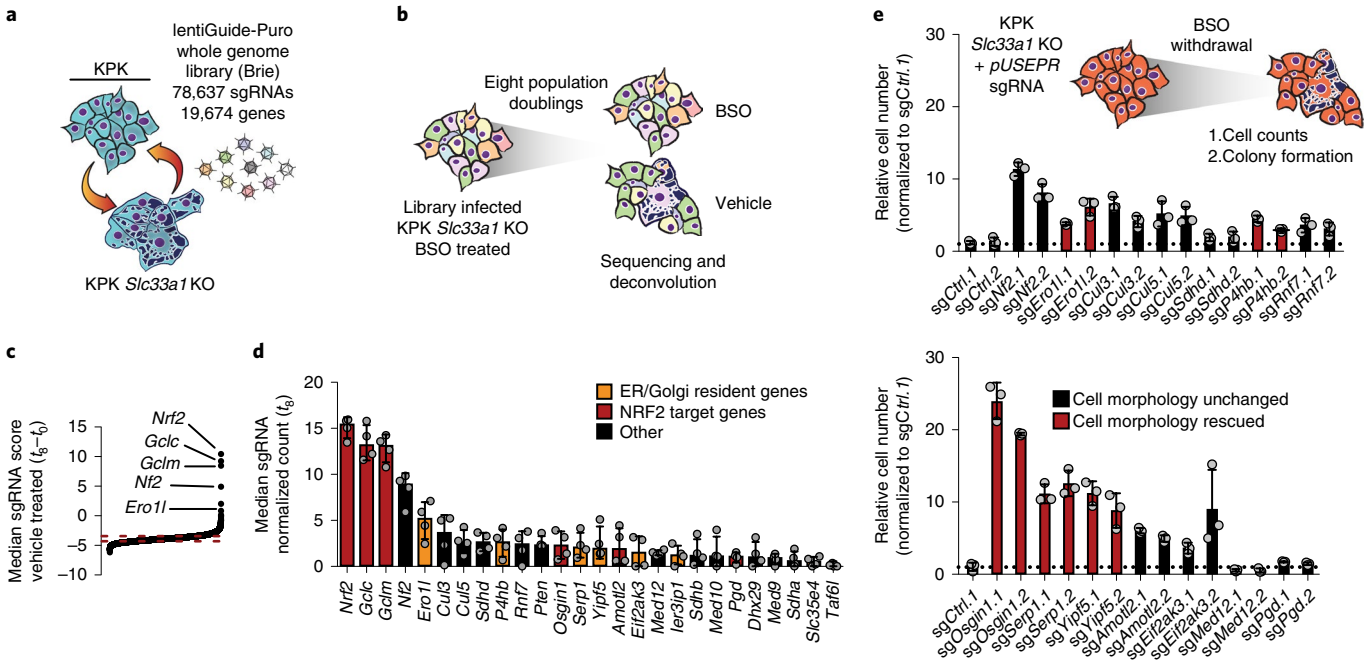

Fig. 7 | Genome-wide CRISPR screen identifies suppressors of *Slc33a1* deficiency. a, Schematic of screen conditions. KPK-*Slc33a1* knockout (KO) cells were generated and infected with the Brie library to identify hits that rescue *Slc33a1* dependency. **b**, Schematic representing screen conditions. KPK-*Slc33a1* knockout cells were infected with Brie library in the presence of BSO and subsequently placed in BSO- or vehicle-treated conditions for eight cumulative population doublings. **c**, Ranked median GSs of genes in the Brie library that passed all thresholds (see Methods). Dotted lines in red represent the spread of control sgRNAs and mark the 25th and 75th GS percentile boundaries. **d**, Waterfall plot of normalized median sgRNA counts ($n=4$) across $n=3$ independent culture wells at t_8. The median is plotted and the error bars denote s.d. **e**, Upper scheme denotes the strategy for the validation pipeline. Bottom portion shows relative cell numbers post-infection with pUSEPR. Cell morphology related to Extended Data Fig. 10a. Data are from $n=3$ biologically independent experiments. Error bars represent mean ± s.d. Data for experiments **e**–**g** are available as source data (Source Data Extended Data Fig. 6).

ER-resident oxidoreductase 1A (*Ero1l*), protein disulfide isomerase 1a (*Pdia*/*P4hb*) and the NRF2 target genes *Osgin1*, *Amotl2* and *Pgd*[52] (Fig. 7d). *PGD* has been implicated in ER homeostasis via modulation of GSH synthesis[53]. GS values of top enriched genes were decreased in BSO-treated samples (Extended Data Fig. 9d,e).

To validate the top enriched candidate genes and investigate the underlying biology that might link the observed dependency associated with targeting *Slc33a1*, *Suco* and *Tapt1*, we transduced KPK-*Slc33a1*, KPK-*Suco* and KPK-*Tapt1* knockout cells with lentiviruses encoding two independent top-scoring sgRNAs from this screen and assessed growth and phenotypic consequences post-BSO withdrawal. Notably, loss of most candidate genes rescued the growth of *Slc33a1*-deficient cells, but not *Suco*- or *Tapt1*-deficient cells (Fig. 7e and Extended Data Fig. 9f). Although *Nf2*, *Cul3*, *Cul5*, *Rnf7*, *Amotl2* and *Eif2ak3* (Perk) sgRNAs rescued the growth of KPK-*Slc33a1* cells, *Ero1l*, *P4hb*, *Osgin1*, *Serp1* and *Yipf5* sgRNAs rescued both the growth and blebbing phenotype associated with *Slc33a1* loss (Extended Data Fig. 10a). Moreover, *Ero1l*, *P4hb*, *Serp1* and *Yipf5* are known ER-resident genes, supporting our observation that KPK cells have a dysfunctional ER. Loss of *Osgin1* also rescued the growth and phenotype of *Slc33a1*-deficient cells, suggesting that genes downstream of NRF2 might contribute to *Slc33a1* dependency (Fig. 7e, Extended Data Fig. 9f and Extended Data Fig. 10a). Furthermore, *Suco* and *Tapt1* knockout cells were rescued only by sgRNAs targeting *Nf2*, *Cul5*, *Rnf7*, *Osgin1* and *Pgd*, suggesting that *Suco* and *Tapt1* dependency is biologically distinct from *Slc33a1* dependency but overlaps in redox biology via rescue through GCLC inhibition (Fig. 3b, Fig. 7e and Extended Data Fig. 9f). In summary, these data suggest that *Slc33a1* loss results in a dysfunctional ER state that affects the growth of *Keap1*-mutant cells. ERO1L is positively regulated by GSH to generate oxidation events used by P4HB for proper protein folding[54,55]. Therefore, loss of either gene is predicted to result in decreased ER oxidation or decreased GSSG production, raising the possibility that SLC33A1 may be involved in regulating ER redox potentials.

Discussion

We have demonstrated that *Keap1* mutation results in increased NRF2-dependent vulnerability to *Slc33a1*, *Suco* and *Tapt1* loss. Although several studies have identified putative *KEAP1*/*NRF2*-mutant-specific synthetic lethal interactions that could be exploited for therapeutic purposes[14,15,17,56,57], all studies so far have been limited in scale (for example, focused on interrogating canonical NRF2 target genes as candidate synthetic lethal factors) and do not rule out the possibility that more comprehensive and systematic queries using increasingly complex functional genomic approaches will uncover new factors that could be targeted for therapeutic benefit. Although we focused this study on *Slc33a1*, we hypothesize that *Keap1*-mutant cells are universally sensitive to dysfunction of an ER stress pathway, of which *Slc33a1* loss imposes the largest selective disadvantage. In line with this observation, we demonstrate increased dependency for endomembrane-associated genes *SUCO* and *TAPT1* (ref. [30]) in *KEAP1*-mutant human cancer cell lines observed in DepMap, which we validated in our murine *Keap1*-mutant cell lines. While *SLC33A1* mutations are associated with developmental defects and childhood mortality, suggestive of a critical role in development[41], pooled genetic screens in embryonic and cancer cell lines suggest that *SLC33A1* is not a pan-essential gene[58,59]. Consistently, we demonstrate that the dependency of *Keap1*-mutant cancer cells on *Slc33a1* can be rescued by loss of several genes with roles in the integrated stress response network. Specifically, loss of ER-resident genes *Erol1*, *P4hb*, *Serp1* and *Yipf5*

or NRF2 target genes *Gclc*, *Gclm* and *Osgin1* rescue both the growth disadvantage and cellular morphology associated with *Slc33a1* loss in NRF2-hyperactivated cells. Although the direct link between GSH and *SLC33A1*, *SUCO* and *TAPT1* remains unclear, we hypothesize that the ER of *Keap1*-mutant cells have been shifted into a dysfunctional state that likely increases proteotoxic stress due to challenges in protein folding that can be rescued by decreasing ER-specific oxidation or ER-specific GSSG production. Consistently with this idea, we observe increased intracellular GSSG upon *Slc33a1* loss in *Keap1*-mutant cells. However, ER-specific accumulation of GSSG upon SLC33A1 inhibition remains to be experimentally validated and other mechanisms might underlie the dependence of *KEAP1*-mutant cells on SLC33A1 and other ER-resident proteins.

Our results are particularly interesting in light of a recent meta-analysis in human cancer cell lines identifying a presumed connection between *SLC33A1* dependency, the NRF2 pathway and high GSH[60]. We showed that *Slc33a1* dependency is rescued via inhibition of GSH synthesis. Using a preclinical *Kras*-mutant GEMM of LUAD, we demonstrate that *Slc33a1* is a robust *Keap1*-mutant specific dependency, validating the cell-autonomous requirement for *Slc33a1* function in this genetic subtype. Overall, our study provides a strong rationale for substratification of patients harboring *KEAP1*-mutant or NRF2-hyperactivated tumors as likely responders to SLC33A1 inhibition and underscore the value of integrating functional genetic approaches with GEMMs to identify and validate genotype-specific therapeutic targets.

Methods

Mice. Animal studies were approved by the Massachusetts Institute of Technology (MIT) Institutional Animal Care and Use Committee. *Kras*$^{LSL\text{-}G12D}$ and *Trp53*$^{fl/fl}$ mice have been described previously[46,47]. *Keap1*$^{fl/fl}$ mice were generated and shared by S. Biswal[49]. All studies employed ≥3 animals per genotype per experimental cohort. Mice were maintained on a mixed C57BL/6:SV129 genetic background. For tumor initiation studies, 8–10-week-old animals with appropriate genotypes were randomized and infected intratracheally with 20,000 transduction units of pUSEC-sg*Olfr102* (sg*Ctrl*) or pUSEC-sg*Slc33a1* lentiviruses as described[43]. Tumor-containing lung area was measured on H&E slides. Histological quantification of lung tumor burden by grade was performed by an automated deep neural network (unpublished) developed by Aiforia Technologies in collaboration with the Tammela and Jacks laboratories and in consultation with veterinarian pathologist R. Bronson. Animals lacking detectable tumors by histopathology were excluded from analyses to ensure that all animals were infected with pUSEC lentiviruses. For allograft and xenograft experiments, 1E6 pUSEPR-infected cells in 100 µl 50% PBS 0.5 mM EDTA and 50% Matrigel were injected into the flanks of immunocompromised mice. For doxycycline-inducible shRNA transplant experiments, 500E5 LVt-TSTOP infected cells in 100 µl of PBS were injected into the flanks of immunocompromised mice. Mice were placed on doxycycline chow when tumors reached 10–20 mm^3. Subcutaneous tumor volumes (mm^3) were calculated using the formula: $(a^2 \times b) \times (\pi/6)$, where a and b are the smaller and larger dimensions, respectively. Eight-week female J/Nu mice (Jackson 007850) were used for all transplant experiments.

Cell culture. HEK293T (American Type Culture Collection (ATCC)) cells were maintained in DMEM (Corning 10-013-CV) supplemented with 10% fetal bovine serum, 2 mM L-glutamine (Gibco 25030) and 50 µg ml^{-1} gentamycin (Gibco 15710). KP cell lines have been described elsewhere[14]. Human cell lines were acquired from ATCC and grown according to ATCC guidelines. All lines tested negative for *Mycoplasma*. Cell lines transduced with Cas9 cDNA remained under blasticidin selection (10 µg ml^{-1}). Cells were treated with inhibitors: BSO (Sigma Aldrich), auranofin (TOCRIS bioscience), erastin (Sigma Aldrich), NAC (Sigma Aldrich) and DMG (Sigma Aldrich) at concentrations denoted in figure legends. Viability was assessed by Cell Titer Glo (Promega G7570). Plates were quantified using a Tecan infinite M200 Pro plate reader or a SpectraMax M5 Microplate reader (Molecular Devices). For clonogenic and low-density assays, cells were stained with crystal violet solution (25% methanol and 75% H_2O) and images were analyzed using ImageJ.

Design and cloning of the druggable genome sgRNA library. See elsewhere[21] for more information on gene selection and library cloning.

Infection of cells with the druggable genome library. All transductions were performed by spin-infection at 1,500 r.p.m. for 2 h at room temperature. 2E6 KP or KPK cells were spin-infected in 12-well plates with viral supernatant at a multiplicity of infection (MOI) of 0.3 and incubated at 37 °C overnight. Viral titers for each cell line were calculated by transduction with decreasing volumes of viral supernatant, selection with 6 µg ml^{-1} puromycin (Gibco A11138) for 24 h and quantification of live cell numbers (normalized to a control, unselected sample).

For the screen, ≥20×10^6 cells were maintained at each step to ensure ≥1,000× representation. A total of 200×10^6 cells were transduced with the sgRNA library in 12-well plates at an MOI of 0.3, then pooled into 15-cm dishes the next day. At 24 h after replating, 100×10^6 cells were pelleted and stored at −80 °C (t_0 population). Then, 100×10^6 cells were selected with 6 µg ml^{-1} puromycin for 24 h. Cells were passaged every 2 d, and 20×10^6 cells were plated after each passage. After eight population doublings (t_8), 20×10^6 cells were pelleted and stored at −80 °C.

Infection of cells with Brie library. Brie library was obtained from Addgene (cat. no. 73633). Five KPK-*Slc33a1* western blot-validated knockout clones were pooled and transduced as described above. For the enrichment screen, a minimum of 5×10^6 cells was maintained at each step to ensure ≥50× representation. Three independent Brie library transductions (MOI ~0.3) were performed as described above using medium containing 50 µM BSO. Each 12-well plate containing a single biological replicate was pooled post-infection into 15-cm dishes containing 50 µM BSO the next day. At 48 h after infection, cells were selected with puromycin for 48 h. Following selection, 5×10^6 cells per independent transduction were collected for t_0 sgRNA representation and 5×10^6 cells were plated into vehicle (water; six replicates) or 50 µM BSO (three replicates) for the duration of the experiment. Cells were passaged upon reaching confluency and 5×10^6 cells were plated after each passage to maintain 50× library representation. After eight population doublings (t_8), 10×10^6 cells were pelleted and stored at −80 °C.

Genomic DNA isolation. Genomic DNA isolation was performed as described previously[21].

Screen deconvolution and analysis (druggable genome library). Integrated sgRNAs were amplified by PCR to attach sequencing adapters and barcodes, as described previously[51]. In brief, a mix of 1 P5_XPR/LKO1 forward primers and 15 P7-index reverse primers (Supplementary Table 11) was used to amplify sgRNAs from each genomic DNA sample using TaKaRa Ex Taq DNA polymerase (RR001C) with 25 cycles at 62 °C annealing temperature. Assuming that each cell contains approximately 6.6 pg of genomic DNA[61], 160 µg (>20 million cells) and 720 µg (>100 million cells) of genomic DNA were used as template for t_8 samples and t_0 samples, respectively. PCR products of 350 bp in length were size-selected on 2% agarose and purified using QIAquick Gel Extraction (QIAGEN, 28704). Samples were sequenced on Illumina NextSeq (75-nt single end reads) at the MIT BioMicro Center.

Sequencing results were analyzed using R (v.3.1.1; www.r-project.org). Flanking adaptor sequences were stripped to retrieve sgRNA target sequences from FASTQ files. Target sequences were collapsed by identity and quantified in terms of exact matches to library sequences. Sequencing read counts per sample were normalized to the total number of reads to yield counts per million sequences, followed by a $\log_2$ transformation[51].

The $\log_2$ fold change score for each sgRNA (sgRNA score) was calculated as the difference between t_8 and t_0 $\log_2$-transformed counts. GSs were then calculated as the median of the four sgRNA scores associated with each gene[62]. Differential GSs for each isogenic pair were calculated by subtracting KP-line GSs from KPK-line GSs. To determine thresholds for significant differentially depleted genes in KPK versus KP cell-line pairs, 500 control sgRNAs were randomly binned into groups of four, median $\log_2$ fold change of t_8 versus t_0 sgRNA read counts were calculated and differential GSs were calculated for these 'pseudogenes'. This process was repeated 10,000 times to define a confident range of possible pseudogene differential GSs and thresholds were set at the lower 5% of scores (FDR = 0.05, −0.64 in pair 1 and −0.63 in pair 2). To filter out genes substantially depleting in KP lines, only genes with scores above the median GSs of all essential genes (defined as the union of two previously described essential gene sets[27,63,64]; Supplementary Table 1) in each KP line (−1.77 in KP1, −2.25 in KP2) were included. To ensure that identified genes were significantly depleted in KPK lines (rather than enriched in KP lines but neutral in KPK lines), the population of pseudogene scores determined previously was used to set thresholds for significant depletion in the KPK lines (FDR = 0.05, −0.43 in KPK1, −0.34 in KPK2). Genes with scores above these thresholds in the KPK lines were excluded. Finally, we excluded essential genes from the analysis[27,63,64].

Screen deconvolution and analysis (Brie library). Integrated sgRNAs were amplified by PCR as described above. A total of 1 µg of genomic DNA was used as a template for t_0 and t_8 samples. All samples were sequenced on Illumina NextSeq (75-nt single end reads) with 50% Phi-X at the MIT BioMicro Center. Sequencing results were analyzed using R (v.3.1.1, www.r-project.org) essentially as described above with the exception that differential GS were calculated by subtracting median BSO-treated GSs from median vehicle-treated GSs. Thresholds set for Brie screen analysis were for t_8 analysis, all sgRNAs with a normalized sgRNA count of 0 at t_0 across two or more replicates were removed from the analysis. Genes for which ≥2 sgRNAs met these criteria across all replicates were used for further analysis. For GS analysis, to determine thresholds for significantly enriched genes in the t_8 samples, we isolated all control sgRNAs and binned them into pseudogenes as described above. With the control

pseudogene scores, we defined the upper and lower boundaries as the 25th percentile (GS = −3.445) and 75th percentile (GS = −4.311). Genes falling above the 25th percentile threshold were deemed significantly enriched in the dataset compared to the spread of the pseudogene scores. Finally, we excluded essential genes from the analysis[27,63,64].

In vitro competition assays. For in vitro competition assays, lentiviral vectors expressing a target sgRNA together with mNeonGreen (pUSPmNG) or tagRFP-P2A-Puro (pUSEPR) were generated by Gibson assembly[65]. The sgRNAs were cloned into the BsmBI-digested pUSPmNG or pUSEPR vectors, as previously described[66]. Dual sgRNA sequences were ordered as a gBlock gene fragment (Integrated DNA Technologies) containing an sgRNA (no. 1) H1 sgRNA (no. 2) cassette flanked by BsmBI-digestion sites. Dual sgRNA sequences were BsmBI-digested and cloned into BsmBI-digested pUSPmNG or pUSEPR vectors. Cas9-expressing cells were infected with sgRNA-expressing pUSPmNG or pUSEPR vectors at a MOI of ~0.5. The percentage of mNeonGreen/tagRFP$^+$ cells was quantified longitudinally via Guava easyCyte HT flow cytometer (Millipore). For each sgRNA, the percentage of mNeonGreen/tagRFP$^+$ cells was normalized to respective values at 2 d after infection.

Colony-formation assays Brie library. Cells were infected at a high MOI with pUSEPR-sgRNA constructs by spinfection in a 12-well plate as described above. Cells were selected and maintained in BSO as described above. After infection, cells were withdrawn from BSO and plated onto six-well plates. Cells were passaged at day 7 to continue timepoint analysis. At day 14, pictures were taken using a Nikon Eclipse Ti2 microscope at ×20 magnification. At day 15, plates were processed for crystal violet staining.

RNA knockdown studies. Lentiviral vectors encoding TRE3GS-mScarlet-miR 30a-hPGK-TetOne-P2A-Puro (LVt-TSTOP) were generated by Gibson assembly[65]. TRE3GS promoter and TetOne (rtTA) sequences were PCR amplified from Clontech plasmid pLVX-TetOne inducible expression systems (cat. no. 631844). The 97-mer sequences targeting *Renilla* and *Slc33a1* were obtained from http://splashrna.mskcc.org/ and cloned as previously described[67] (Supplementary Table 11). Cells were infected with a MOI of 0.5 and selected in puromycin (6 μg ml^{-1}). Medium containing doxycycline (Sigma D9891; 10 ng ml^{-1}) was replenished every 2 d for 7 d and cells were passaged in presence or absence of BSO (50 μM). CRISPR-interference (CRISPRi) constructs were obtained from Addgene (71236). The sgRNAs targeting *Slc33a1* or *Olfr102* were obtained from published whole-genome CRISPRi datasets[68].

Immunoblotting. Cells were lysed in 250 μl of ice-cold RIPA buffer (Pierce, 89900) supplemented with 1× Complete Mini inhibitor mixture (Roche, 11836153001) and mixed on a rotator at 4 °C for 30 min. Protein concentration was quantified using the Bio-Rad DC protein assay (cat. no. 500-0114). Then, 30–50 μg of total protein was separated on 4–12% Bis-Tris gradient gels (Bio-Rad) by SDS–PAGE and then transferred to nitrocellulose membranes. The following antibodies were used for immunoblotting following manufacturer suggested protocols: anti-GAPDH (Santa Cruz, sc-25778, 1:500 dilution), anti-HSP90 (BD, 610418, 1:10,000 dilution), anti-NRF2 (Santa Cruz, sc-722, 1:200 dilution), anti-KEAP1 (CST, 8047, 1:1,000 dilution), anti-GCLC (Santa Cruz, sc-22755, 1:200 dilution), anti-p62 (CST 23214, 1:1,000 dilution), anti-LC3 (CST 12741, 1:1,000 dilution), anti-BECLIN (CST 3495, 1:1,000 dilution), anti-pS6K T421/424 (CST 9204, 1:1,000 dilution), anti-BiP (CST 3177, 1:1,000 dilution), anti-FLAG (CST 14793, 1:1,000 dilution), anti-HH3 (CST 4499, 1:1,000 dilution), anti-GCN2 (CST 65981S, 1:1,000 dilution), anti-PERK (CST 5683S, 1:1,000 dilution), anti-ATF4 (CST 11815S, 1:1,000 dilution), anti-eIF2a (CST 5324S, 1:2,000 dilution), anti-phospho-eIF2a S51 (CST 3398S, 1:1,000 dilution), anti-SLC33A1 (Sigma HPA042430, 1:1,000 dilution), anti-mouse HRP (CST 7076, 1:10,000 dilution) and anti-rabbit HRP (CST 7074, 1:10,000 dilution). Anti-SLC33A1 antibody was cross-validated with anti-HA antibody in C-terminal HA-tagged SLC33A1 expressing 293Ts blotted in parallel with KPK-sgSlc33a1-targeted clones.

Immunohistochemistry and immunofluorescence. Mice were killed by CO_2 asphyxiation. Lungs were perfused through the trachea with 4% paraformaldehyde, fixed overnight, transferred to 70% ethanol and embedded in paraffin. Sections were cut to 4 μm and stained with H&E. Chromogenic IHC was performed on a Ventana Medical Systems Discovery XT instrument with online deparaffinization using Ventana's reagents and detection kits. Antigens were retrieved in Ventana Cell Conditioner 1 or 2. The following antibodies were used for IHC as per manufacturer protocols: anti-pHH3 (Ser10; Cell Signaling, 9701, 1:200 dilution), anti-NQO1 (Sigma Aldrich, HPA007308, 1:200 dilution). HRP detection was used for NQO1 and pHH3. NQO1 and pHH3 were antigen retrieved in Ventana Cell Conditioner 1 (Tris-Borate-EDTA). Pictures were obtained using a digital whole-slide scanner Leica SCN400F and Slidepath software v.4.0.8.

Lentiviral production. Lentiviruses were produced by co-transfection of 293T cells (ATCC) with lentiviral backbone constructs and packaging vectors (psPAX2 and pMD2.G; Addgene 12260 and 12259) using TransIT-LT1 (Mirus Bio MR 2306). Virus was concentrated as previously described[14].

DepMap analysis. All data analyzed were accessed from the Broad Institute (www.depmap.org) whole-genome CRISPR screens[64]. Gene coessentiality datasets were obtained from elsewhere[28]. Ranking DepMap cell lines by their transcriptional correlation with the NRF2 core target gene set (and the *KEAP1*-mutant signature) was performed using single-sample GSEA[69]. Separately, to search for targets that correlate well with *NRF2* dependence, the Pearson correlation coefficient was calculated between select genes and every other gene. The genetic background of DepMap cell lines was assessed from mutational data made available by the Cancer Cell Line Encyclopedia. Results of these analyses were used to compare CERES scores between *KEAP1/NRF2*-mutant lines versus wild-type lines, as well as across the ranked list of cell lines based on their transcriptional correlation with the NRF2 core gene set.

Transcriptome analysis. RNA was collected from cells with the RNeasy Plus Mini kit (QIAGEN) as described previously[14]. For real-time qPCR analysis, cDNA was synthesized from RNA with the High-Capacity cDNA Reverse Transcription kit (Applied Biosystems 4368814). Genes *Gclc*, *Nqo1*, *Atf4*, *Hspa5*, *Xpb1s* and *Ddit3* were analyzed by quantitative reverse transcription PCR on LightCycler 480 II (Roche) using RT–qPCR primers (Supplementary Table 11).

Extracellular flux measurements. Extracellular flux measurements were calculated by extracting fresh and spent medium supernatant from tracing experiments after 24 h of growth. Cells were assumed to grow exponentially over the culture period. Metabolites were measured using YSI biochemistry analyzer (Yellow Springs Instruments).

Liquid chromatography–mass spectrometry (LC–MS) analysis. Independently pUSEPR-infected cells were seeded in DMEM supplemented with 10% dialyzed FBS at 1 ml per well containing 50 μM BSO in six-well plates. The following day, 2 ml of fresh DMEM was added to each well with or without 50 μM BSO. At 48 h after replenishment of medium, cell numbers were counted for duplicate sets of BSO-treated and untreated samples (three wells per condition). Samples were washed twice with 4 ml of ice-cold blood bank saline (Azer Scientific, ES1244G) and extracted on ice using ice-cold methanol:water (80:20) containing norvaline. Extracts were collected, transferred to 1.5-ml tubes, vortexed at maximum speed for 15 min at 4 °C, then centrifuged at 13,000 r.p.m. for 10 min at 4 °C. The supernatant was collected, transferred to a new 1.5-ml tube, then evaporated to dryness under nitrogen. Samples were analyzed by LC–MS (Whitehead Metabolite Profiling Core Facility) as described previously[70].

Glutathione measurements. GSH and GSSG was measured with a GSH/GSSG-Glo assay kit (V6611, Promega) for the indicated amount of time.

Bioinformatic analysis of CRISPR-targeted loci. For PCR amplicons, 150–300-bp paired-end reads were used in downstream analyses. The reference sequence of the target locus supplemented with 10-bp genomic flanks was indexed using an enhanced suffix array[71]. Read ends were anchored in the reference sequence using 10-bp terminal segments for a suffix array index lookup to search for exact matches. A sliding window of unit step size and a maximal soft-clip limit of 10 bp was used to search for possible anchors at either end of each read. Optimal Smith–Waterman dynamic programming alignment[72] was performed between the reduced state space of the read sequence and corresponding reference sequence, spanning maximally distanced anchor locations. Scoring parameters were selected to allow for sensitive detection of short and long insertions and deletions, while allowing for up to four mismatches and the highest scoring alignment was selected. Read pairs with both reads aligned in the proper orientation were processed to summarize the number of wild-type reads and the location and size of each insertion and deletion event. Overlapping reads within pairs were both required to support the event if they overlapped across the event location. Additionally, mutation events and wild-type reads were summarized within the extents of the sgRNA sequence and protospacer-adjacent motif (PAM) site by considering read alignments that had a minimum of a 20-bp overlap with this region. Mutation calls were translated to genomic coordinates and subsequently annotated using Annovar[73]. The alignment and post-processing code was implemented in C++ along with library functions from SeqAn[74] and SSW and utility functions in Perl and R (www.R-project.org). Mutation calls were subjected to manual review using the Integrated Genomics Viewer[75].

Gene expression signature analyses. Illumina HiSeq 2000 50-nt single-ended reads were mapped to the University of California, Santa Cruz mm9 mouse genome build (http://genome.ucsc.edu/) using RSEM[76]. Raw estimated expression counts were upper-quartile normalized to a count of 1,000 (ref. [77]). *Keap1*-mutant ($n = 2$), wild-type ($n = 2$) and wild-type + sg*Slc33a1* transduced ($n = 2$) samples were jointly analyzed to derive a murine signature of *Slc33a1*-mutant gene expression changes. Given the complexity of the database in terms of a mixture of genotypes and treatment, a high-resolution signature discovery approach (independent component analysis) was employed to characterize global gene expression profiles, essentially as described previously[14]. R implementation of the core JADE (joint approximate diagonalization of eigenmatrices) algorithm[78] was used along with custom R utilities. Statistical significance of biologically relevant signatures was assessed using a Mann–Whitney *U*-test ($\alpha = 0.05$). A murine *Slc33a1*-mutant

signature was derived from this analysis, identifying genes with a differential expression pattern between wild-type and all other samples. All RNA-seq analyses were conducted in the R Statistical Programming language (http://www.r-project.org/). GSEA was carried out using the preranked mode with default settings[79,80]. This *Slc33a1* knockout signature was compared to publicly available datasets[33].

Statistics and reproducibility. We used GraphPad Prism software v.6.03 for statistical analyses. Variance was similar between compared groups and *P* values were determined by two-tailed Student's *t*-test for all measurements comparing untreated to treated samples of single time points. Two-sided Mann–Whitney *U*-test with Holm's multiple comparisons testing was used for tumor burden and grade quantifications. ANOVA with Tukey's post hoc test was used for comparisons between multiple groups. For analysis between groups over multiple time measurements (growth curves), two-way ANOVA was used with appropriate multiple comparisons tests listed in figure legends. Figure legends denominate statistical analysis used. No statistical method was used to predetermine sample size. GEMMs induced with pUSEC lentiviruses lacking any detectable burden by H&E were excluded from this analysis to not skew the results toward artificially lower tumor burden. No other data were excluded from this study. Investigators were not blinded to allocation during experiments and outcome assessment, except for mouse studies.

Reporting summary. Further information on research design is available in the Nature Research Reporting Summary linked to this article.

Data availability

RNA-seq data from this study have been deposited in the Gene Expression Omnibus under accession code GSE145945. CRISPR screen and target locus sequence datasets have been submitted to the Sequence Read Archive and are available under BioProject ID PRJNA611102. DepMap datasets analyzed here can be found in elsewhere[64]. Unedited western blots have been provided as Source Data Figs. 1 and 2. MS data have been deposited in MetaboLights with the primary accession code MTBLS1647. Numerical source data for Main and Extended Data Figures are provided as Source Data Extended Data Figs. 1–6. All other data supporting the findings of this study are available from the corresponding author on reasonable request.

Code availability

Bioinformatic analyses were performed using open-source software, including RSEM v.1.2.12 (ref. [76]), JADE v.1.1.0, Annovar v.2016-02-01 (ref. [73]), SeqAn v.2.0.1 (ref. [74]) and SSW v.0.1.4, as well as in-house scripts in R that are available from the corresponding author on reasonable request.

Received: 18 July 2019; Accepted: 1 May 2020;
Published online: 8 June 2020

References

1. Shen, R. et al. Harnessing clinical sequencing data for survival stratification of patients with metastatic lung adenocarcinomas. *JCO Precis. Oncol.* **3** (2019).
2. Jaramillo, M. C. & Zhang, D. D. The emerging role of the Nrf2-Keap1 signaling pathway in cancer. *Genes Dev.* **27**, 2179–2191 (2013).
3. TCGA, L. U. A. D. et al. Comprehensive molecular profiling of lung adenocarcinoma. *Nature* **511**, 543–550 (2014).
4. Berger, A. H. et al. High-throughput phenotyping of lung cancer somatic mutations. *Cancer Cell* **30**, 214–228 (2016).
5. Hammerman, P. S. et al. Comprehensive genomic characterization of squamous cell lung cancers. *Nature* **489**, 519–525 (2012).
6. Hast, B. E. et al. Cancer-derived mutations in KEAP1 impair NRF2 degradation but not ubiquitination. *Cancer Res.* **74**, 808–817 (2014).
7. Rojo de la Vega, M., Chapman, E. & Zhang, D. D. NRF2 and the hallmarks of cancer. *Cancer Cell* **34**, 21–43 (2018).
8. Itoh, K., Mimura, J. & Yamamoto, M. Discovery of the negative regulator of Nrf2, Keap1: A historical overview. *Antioxid. Redox Signal.* **13**, 1665–1678 (2010).
9. Harris, I. S. & DeNicola, G. M. The Complex Interplay between Antioxidants and ROS in Cancer. *Trends Cell Biol.* **30**, 440–451 (2020).
10. Wu, W. L. & Papagiannakopoulos, T. The Pleiotropic Role of the KEAP1/NRF2 Pathway in Cancer. *Annu. Rev. Cancer Biol.* **4**, 413–435 (2020).
11. Todoric, J. et al. Stress-Activated NRF2-MDM2 Cascade Controls Neoplastic Progression in Pancreas. *Cancer Cell* **32**, 824–839.e8 (2017).
12. Chio, I. I. C. et al. NRF2 Promotes Tumor Maintenance by Modulating mRNA Translation in Pancreatic Cancer. *Cell* **166**, 963–976 (2016).
13. DeNicola, G. M. et al. Oncogene-induced Nrf2 transcription promotes ROS detoxification and tumorigenesis. *Nature* **475**, 106–110 (2011).
14. Romero, R. et al. Keap1 loss promotes Kras-driven lung cancer and results in dependence on glutaminolysis. *Nat. Med.* **23**, 1362–1368 (2017).
15. Sayin, V. I. et al. Activation of the NRF2 antioxidant program generates an imbalance in central carbon metabolism in cancer. *eLife* **6**, 1–23 (2017).
16. DeNicola, G. M. et al. NRF2 regulates serine biosynthesis in non-small cell lung cancer. *Nat. Genet.* **47**, 1475–1481 (2015).
17. Kang, Y. P. et al. Cysteine dioxygenase 1 is a metabolic liability for non-small cell lung cancer. *eLife* **8** (2019).
18. Mitsuishi, Y. et al. Nrf2 Redirects Glucose and Glutamine into Anabolic Pathways in Metabolic Reprogramming. *Cancer Cell* **22**, 66–79 (2012).
19. LeBoeuf, S. E. et al. Activation of Oxidative Stress Response in Cancer Generates a Druggable Dependency on Exogenous Non-essential Amino Acids. *Cell Metab.* (2019).
20. Lignitto, L. et al. Nrf2 Activation Promotes Lung Cancer Metastasis by Inhibiting the Degradation of Bach1. *Cell* **178**, 316–329.e18 (2019).
21. Li, L. et al. Identification of DHODH as a therapeutic target in small cell lung cancer. *Sci. Transl. Med.* **11**, eaaw7852 (2019).
22. Pasetto, M. et al. Whole-genome RNAi screen highlights components of the endoplasmic reticulum/Golgi as a source of resistance to immunotoxin-mediated cytotoxicity. *Proc. Natl Acad. Sci.* **112**, E1135–E1142 (2015).
23. Cui, J. et al. Competitive Inhibition of the Endoplasmic Reticulum Signal Peptidase by Non-cleavable Mutant Preprotein Cargos. *J. Biol. Chem.* **290**, 28131–28140 (2015).
24. Yamamori, T., Meike, S., Nagane, M., Yasui, H. & Inanami, O. ER stress suppresses DNA double-strand break repair and sensitizes tumor cells to ionizing radiation by stimulating proteasomal degradation of Rad51. *FEBS Lett.* **587**, 3348–3353 (2013).
25. Liu, Y. et al. Activation of the Unfolded Protein Response via Inhibition of Protein Disulfide Isomerase Decreases the Capacity for DNA Repair to Sensitize Glioblastoma to Radiotherapy. *Cancer Res.* **79**, 2923–2932 (2019).
26. Cloer, E. W. et al. p62-Dependent Phase Separation of Patient-Derived KEAP1 Mutations and NRF2. *Mol. Cell. Biol.* **38**, (2018).
27. Meyers, R. M. et al. Computational correction of copy number effect improves specificity of CRISPR–Cas9 essentiality screens in cancer cells. *Nat. Genet.* **49**, 1779–1784 (2017).
28. Kim, E. et al. A network of human functional gene interactions from knockout fitness screens in cancer cells. *Life Sci. Alliance* **2**, e201800278 (2019).
29. Igarashi, K. et al. Regulation of transcription by dimerization of erythroid factor NF-E2 p45 with small Maf proteins. *Nature* **367**, 568–572 (1994).
30. Hein, M. Y. et al. A Human Interactome in Three Quantitative Dimensions Organized by Stoichiometries and Abundances. *Cell* **163**, 712–723 (2015).
31. Jonas, M. C., Pehar, M. & Puglielli, L. AT-1 is the ER membrane acetyl-CoA transporter and is essential for cell viability. *J. Cell Sci.* **123**, 3378–3388 (2010).
32. Pehar, M., Jonas, M. C., Hare, T. M. & Puglielli, L. SLC33A1/AT-1 Protein Regulates the Induction of Autophagy Downstream of IRE1/XBP1 Pathway. *J. Biol. Chem.* **287**, 29921–29930 (2012).
33. Adamson, B. et al. A Multiplexed Single-Cell CRISPR Screening Platform Enables Systematic Dissection of the Unfolded Protein Response. *Cell* **167**, 1867–1882.e21 (2016).
34. Meister, A. & Anderson, M. E. Glutathione. *Annu. Rev. Biochem.* **52**, 711–760 (1983).
35. Ponsero, A. J. et al. Endoplasmic Reticulum Transport of Glutathione by Sec61 Is Regulated by Ero1 and Bip. *Mol. Cell* **67**, 962–973.e5 (2017).
36. Griffith, O. W. & Meister, A. Potent and specific inhibition of glutathione synthesis by buthionine sulfoximine (S-n-butyl homocysteine sulfoximine). *J. Biol. Chem.* **254**, 7558–7560 (1979).
37. Dolma, S., Lessnick, S. L., Hahn, W. C. & Stockwell, B. R. Identification of genotype-selective antitumor agents using synthetic lethal chemical screening in engineered human tumor cells. *Cancer Cell* **3**, 285–296 (2003).
38. Criddle, D. N. et al. Menadione-induced Reactive Oxygen Species Generation via Redox Cycling Promotes Apoptosis of Murine Pancreatic Acinar Cells. *J. Biol. Chem.* **281**, 40485–40492 (2006).
39. Marzano, C. et al. Inhibition of thioredoxin reductase by auranofin induces apoptosis in cisplatin-resistant human ovarian cancer cells. *Free Radic. Biol. Med.* **42**, 872–881 (2006).
40. Harris, I. S. et al. Deubiquitinases Maintain Protein Homeostasis and Survival of Cancer Cells upon Glutathione Depletion. *Cell Metab.* **29**, (2019).
41. Peng, Y. et al. Deficient Import of Acetyl-CoA into the ER Lumen Causes Neurodegeneration and Propensity to Infections, Inflammation, and Cancer. *J. Neurosci.* **34**, 6772–6789 (2014).
42. Dieterich, I. A. et al. Acetyl-CoA flux regulates the proteome and acetyl-proteome to maintain intracellular metabolic crosstalk. *Nat. Commun.* **10**, 3929 (2019).
43. DuPage, M., Dooley, A. L. & Jacks, T. Conditional mouse lung cancer models using adenoviral or lentiviral delivery of Cre recombinase. *Nat. Protoc.* **4**, 1064–1072 (2009).
44. Davidson, S. M. et al. Environment Impacts the Metabolic Dependencies of Ras-Driven Non-Small Cell Lung Cancer. *Cell Metab.* **23**, 517–528 (2016).
45. Muir, A. & Vander Heiden, M. G. The nutrient environment affects therapy. *Science* (80-.). **360**, 962–963 (2018).
46. Jackson, E. L. et al. Analysis of lung tumor initiation and progression using conditional expression of oncogenic K-ras. *Genes Dev.* **15**, 3243–3248 (2001).
47. Jackson, E. L. et al. The differential effects of mutant p53 alleles on advanced murine lung cancer. *Cancer Res.* **65**, 10280–10288 (2005).

48. Winslow, M. M. et al. Suppression of lung adenocarcinoma progression by Nkx2-1. *Nature* **473**, 101–104 (2011).
49. Blake, D. J. et al. Deletion of Keap1 in the lung attenuates acute cigarette smoke-induced oxidative stress and inflammation. *Am. J. Respir. Cell Mol. Biol.* **42**, 524–536 (2010).
50. Platt, R. J. et al. CRISPR-Cas9 knockin mice for genome editing and cancer modeling. *Cell* **159**, 440–455 (2014).
51. Doench, J. G. et al. Optimized sgRNA design to maximize activity and minimize off-target effects of CRISPR-Cas9. *Nat. Biotechnol.* **34**, 184–191 (2016).
52. Brennan, M. S., Matos, M. F., Richter, K. E., Li, B. & Scannevin, R. H. The NRF2 transcriptional target, OSGIN1, contributes to monomethyl fumarate-mediated cytoprotection in human astrocytes. *Sci. Rep.* **7**, 42054 (2017).
53. Li, H. et al. 6-Phosphogluconate Dehydrogenase Links Cytosolic Carbohydrate Metabolism to Protein Secretion via Modulation of Glutathione Levels. *Cell Chem. Biol.* **26**, 1306–1314.e5 (2019).
54. Tu, B. P. & Weissman, J. S. Oxidative protein folding in eukaryotes: mechanisms and. *J. Cell Biol.* **164**, 341–346 (2004).
55. Sevier, C. S. & Kaiser, C. A. Ero1 and redox homeostasis in the endoplasmic reticulum. *Biochim. Biophys. Acta - Mol. Cell Res.* **1783**, 549–556 (2008).
56. McMillan, E. A. et al. Chemistry-First Approach for Nomination of Personalized Treatment in Lung Cancer. *Cell* **173**, 864–878.e29 (2018).
57. Bar-Peled, L. et al. Chemical Proteomics Identifies Druggable Vulnerabilities in a Genetically Defined Cancer. *Cell* **171**, 696–709.e23 (2017).
58. Li, M. et al. Genome-wide CRISPR-KO Screen Uncovers mTORC1-Mediated Gsk3 Regulation in Naive Pluripotency Maintenance and Dissolution. *Cell Rep.* **24**, 489–502 (2018).
59. Hart, T. et al. High-Resolution CRISPR Screens Reveal Fitness Genes and Genotype-Specific Cancer Liabilities. *Cell* **163**, 1515–1526 (2015).
60. Li, H. et al. The landscape of cancer cell line metabolism. *Nat. Med.* **25**, 1–11 (2019).
61. Chen, S. et al. Genome-wide CRISPR Screen in a Mouse Model of Tumor Growth and Metastasis. *Cell* **160**, 1246–1260 (2015).
62. Wang, T., Wei, J. J., Sabatini, D. M. & Lander, E. S. Genetic Screens in Human Cells Using the CRISPR-Cas9 System. *Science* (80-.). **343**, 80–84 (2014).
63. Hart, T. et al. Evaluation and Design of Genome-Wide CRISPR/SpCas9 Knockout Screens. *G3 Genes|Genomes|Genetics* **7**, 2719–2727 (2017).
64. DepMap Broad. DepMap Achilles 19Q2 Public. (2019). https://doi.org/10.6084/m9.figshare.8061398.v1
65. Akama-Garren, E. H. et al. A Modular Assembly Platform for Rapid Generation of DNA Constructs. *Sci. Rep.* **6**, 16836 (2016).
66. Sanjana, N. E., Shalem, O. & Zhang, F. Improved vectors and genome-wide libraries for CRISPR screening. *Nat. Methods* **11**, 783–784 (2014).
67. Fellmann, C. et al. An optimized microRNA backbone for effective single-copy RNAi. *Cell Rep.* **5**, 1704–1713 (2013).
68. Horlbeck, M. A. et al. Compact and highly active next-generation libraries for CRISPR-mediated gene repression and activation. *Elife* **5**, 1–20 (2016).
69. Barbie, D. A. et al. Systematic RNA interference reveals that oncogenic KRAS-driven cancers require TBK1. *Nature* **462**, 108–112 (2009).
70. Cantor, J. R. et al. Physiologic Medium Rewires Cellular Metabolism and Reveals Uric Acid as an Endogenous Inhibitor of UMP Synthase. *Cell* **169**, 258–272.e17 (2017).
71. Abouelhoda, M. I., Kurtz, S. & Ohlebusch, E. Replacing suffix trees with enhanced suffix arrays. *J. Discret. Algorithms* **2**, 53–86 (2004).
72. Smith, T. F. & Waterman, M. S. Identification of common molecular subsequences. *J. Mol. Biol.* **147**, 195–197 (1981).
73. Wang, K., Li, M. & Hakonarson, H. ANNOVAR: functional annotation of genetic variants from high-throughput sequencing data. *Nucleic Acids Res.* **38**, e164 (2010).
74. Döring, A., Weese, D., Rausch, T. & Reinert, K. SeqAn An efficient, generic C++ library for sequence analysis. *BMC Bioinformatics* **9**, 11 (2008).
75. Thorvaldsdottir, H., Robinson, J. T. & Mesirov, J. P. Integrative Genomics Viewer (IGV): high-performance genomics data visualization and exploration. *Brief. Bioinform.* **14**, 178–192 (2013).
76. Li, H. & Durbin, R. Fast and accurate short read alignment with Burrows-Wheeler transform. *Bioinformatics* **25**, 1754–1760 (2009).
77. Bullard, J. H., Purdom, E., Hansen, K. D. & Dudoit, S. Evaluation of statistical methods for normalization and differential expression in mRNA-Seq experiments. *BMC Bioinformatics* **11**, 94 (2010).
78. Biton, A. et al. Independent component analysis uncovers the landscape of the bladder tumor transcriptome and reveals insights into luminal and basal subtypes. *Cell Rep.* **9**, 1235–1245 (2014).
79. Subramanian, A. et al. Gene set enrichment analysis: a knowledge-based approach for interpreting genome-wide expression profiles. *Proc. Natl Acad. Sci. USA* **102**, 15545–15550 (2005).
80. Mootha, V. K. et al. PGC-1α-responsive genes involved in oxidative phosphorylation are coordinately downregulated in human diabetes. *Nat. Genet.* **34**, 267–273 (2003).

Acknowledgements

We thank J. Settleman, D. Stokoe, T. Papagiannakopoulos, I. Harris, L. Sullivan, M. Sullivan, Z. Li, G. DeNicola and M. Hemann for scientific discussions and feedback; T. Tammela and T. Westerling for contributions to Aiforia tumor deep neural network analyses; S. Levine for massively parallel sequencing expertise; M. Griffin, M. Jennings and G. Paradis for FACS support; K. Cormier and the Hope Babette Tang (1983) Histology Facility for histology support; B. Chan and the Whitehead Metabolomics core for LC–MS and metabolite analysis; K. Yee, A. Deconinck and J. Teixeira for administrative support; and the Swanson Biotechnology Center for excellent core facilities. This work was supported by the Howard Hughes Medical Institute, Calico Life Sciences and the Koch Institute Support (core) grant P30-CA14051 from the National Cancer Institute (NCI). R.R. was supported by the National Science Foundation Graduate Research Fellowship and the NCI of the National Institutes of Health under award numbers 1122374 and F31CA224796, respectively. P.P.H. is supported in part by the National Cancer Institute of the National Institutes of Health under award number 2T32CA071345-21A1. The content is solely the responsibility of the authors and does not necessarily represent the official views of the National Institutes of Health. M.G.V.H. is a Howard Hughes Medical Institute Faculty Scholar and acknowledges additional support from SU2C, the Ludwig Center for Molecular Oncology at MIT, the MIT Center for Precision Cancer Medicine and the NCI. T.J. is a Howard Hughes Medical Institute Investigator, David H. Koch Professor of Biology and Daniel K. Ludwig Scholar. We apologize for any relevant citations we have missed due to reference limitations.

Author contributions

Author contributions were as follows: R.R., F.J.S.R. and T.J. designed the study; R.R., F.J.S.R., P.M.K.W., K.L.M., T.J.G.R., S.L.R., L.Z.L. and M.C.B. performed experiments; A.B. and P.M.K.W. performed bioinformatic analyses; A.M., P.P.H., C.A.L. and M.G.V.H. provided feedback and interpretation of metabolism data; S.R.N., L.L. and C.I.C. curated and generated the DGL; P.M.K.W. and R.T.B. trained Aiforia deep neural networks for histological assessment of lung tumor burden and grade; S.N. developed the double-sgRNA cloning strategy; R.R., F.J.S.R., P.M.K.W. and T.J. wrote the manuscript with comments from all authors.

Competing interests

M.G.V.H. is a consultant and scientific advisory board member for Agios Pharmaceuticals, Aeglea Biotherapeutics, iTeos and Auron Therapeutics. P.P.H. is a consultant for Auron Therapeutics. T.J. is a member of the Board of Directors of Amgen and Thermo Fisher Scientific. He is also a Co-founder of Dragonfly Therapeutics and T2 Biosystems. T.J. serves on the Scientific Advisory Board of Dragonfly Therapeutics, SQZ Biotech and Skyhawk Therapeutics. None of these affiliations represents a conflict of interest with respect to the design or execution of this study or interpretation of data presented in this manuscript. The laboratory of T.J. currently also receives funding from the Johnson & Johnson Lung Cancer Initiative, but this funding did not support the research described in this manuscript. This work was supported by the Howard Hughes Medical Institute and Calico Life Sciences.

Additional information

Extended data is available for this paper at https://doi.org/10.1038/s43018-020-0071-1.

Supplementary information is available for this paper at https://doi.org/10.1038/s43018-020-0071-1.

Correspondence and requests for materials should be addressed to T.J.

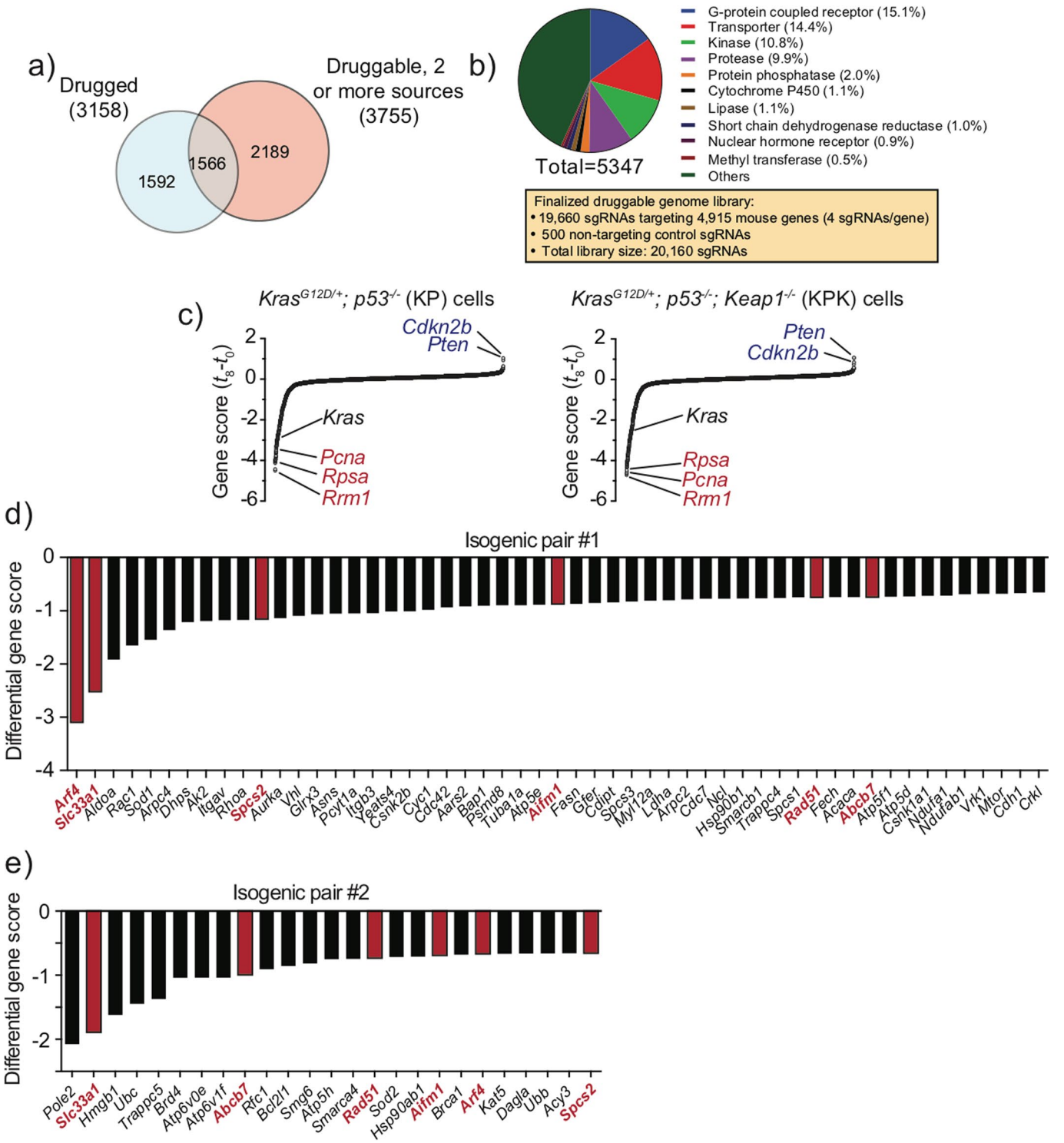

Extended Data Fig. 1 | CRISPR screening platform identifies genotype-specific vulnerabilities in *Keap1*-mutant LUAD cell lines. a, Number of genes in each category in the druggable genome library (DGL). **b**, Composition of genes in the DGL by gene category. Bottom rectangle displays the breakdown of the total number of sgRNAs in the DGL. **c**, Waterfall plots of rank ordered average GSs after 8 doublings (t_8) post infection between both KP cell lines (left) and KPK cell lines (right). Genes in red indicate pan-essential genes. Genes in blue indicate tumor suppressor genes. Data derived from $n = 2$ cell lines per panel. **d**, Ranked differential gene scores (KPK1-KP1 GS, $n = 1$ pair) of the top significantly depleted genes that passed all thresholds (see Methods). Genes marked in red indicate commonly depleted genes in the top ranked list between both isogenic cell line pairs. **e**, Ranked differential gene scores (KPK2-KP2 GS, $n = 1$ pair) of the top significantly depleted genes that passed all thresholds (see Methods). Genes marked in red indicate commonly depleted genes in the top ranked list between both isogenic cell line pairs.

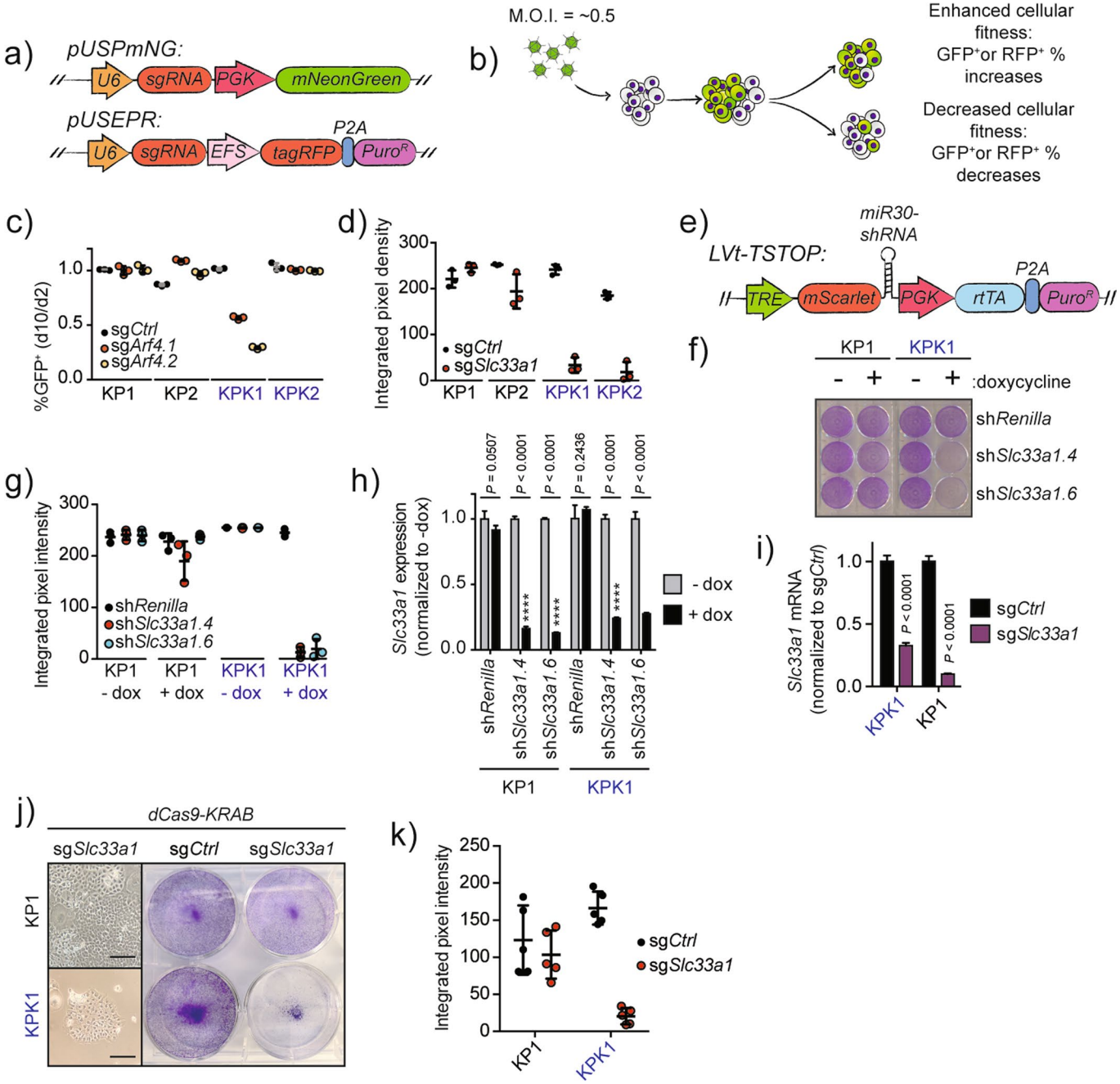

Extended Data Fig. 2 | See neext page for caption.

Extended Data Fig. 2 | *In vitro* validation of *Slc33a1* as a *Keap1*-mutant-specific dependency. a, Schematic of lentiviral vectors utilized for fluorescence competition assays. **b**, Experimental validation pipeline for gene essentiality by fluorescence competition assays. **c**, Fluorescence competition assays of KP or KPK isogenic pairs targeted with sg*Ctrl* or two independent sgRNAs targeting *Arf4*. Plot displays day 2 normalized %GFP + (pUSPmNG) cells at day 10 post infection with sg*Ctrl* or sg*Arf4*. Data are representative of $n = 3$ independent culture wells per cell line per sgRNA. **d**, Quantified colony formation assay via the integrated pixel density assessed by ImageJ software. Related to Fig. 1f. Data are representative of $n = 3$ independent culture wells/cell line/sgRNA. **e**, Schematic of *LVt-TSTOP* lentiviral vector utilized for doxycycline inducible miR30a-based shRNA expression. TRE, tetracycline-response element (TRE3GS); rtTA, reverse tetracycline-controlled transactivator (Tet-On 3 G); P2A; 2 A self-cleaving peptide; Puro, Puromycin-resistance cassette. **f**, Colony formation assay of KP1 and KPK1 cells transduced with LVt-TSTOP vectors expressing sh*Renilla* or sh*Slc33a1*. Data are representative of $n = 3$ independent culture wells per cell line per shRNA. **g**, Quantified colony formation assay via the integrated pixel density assessed by ImageJ software. Related to (**f**). Data are representative of $n = 3$ independent culture wells per cell line per shRNA. **h**, *Slc33a1* expression quantified by qPCR in cells treated with and without doxycycline (10 ng/mL) for 48 hours. Bars represent mRNA expression normalized to *Actb* then to -dox conditions, and the error bars represent mean ± s.d. from the mean across $n = 3$ or 4 independent experiments. *P* values were determined by unpaired two-tailed Student's *t*-test. **i**, *Slc33a1* expression quantified by qPCR 48 hours post-transduction with sgRNA-CRISPRi constructs. Bars represent mRNA expression normalized to *Actb* then to sg*Ctrl* samples, and the error bars represent mean ± s.d. from the mean across $n = 4$ independent experiments. *P* values were determined by unpaired two-tailed Student's *t*-test. **j**, Left: Representative microscopy images of cells transduced with sgRNAs mediating transcriptional repression of the *Slc33a1* promoter (Scale bar = 100 μm). Right: Colony formation assay of dCas9-KRAB expressing cells in the presence of the indicated promoter-targeting sgRNAs. Data are representative of $n = 3$ independent culture wells per cell line per sgRNA. **k**, Quantified colony formation assay via the integrated pixel density assessed by ImageJ software. Related to (**j**). Data are representative of $n = 3$ independent culture wells per cell line per sgRNA. All error bars depicted represent mean ± s.d.. Data from a single experiment are shown in **c, d, f, g, j**, and **k** are representative of two independent experiments with similar results. Data for experiments **c, h**, and **i** are available as source data (Source_Data_Extended_Data_1; Source_Data_Extended_Data_2).

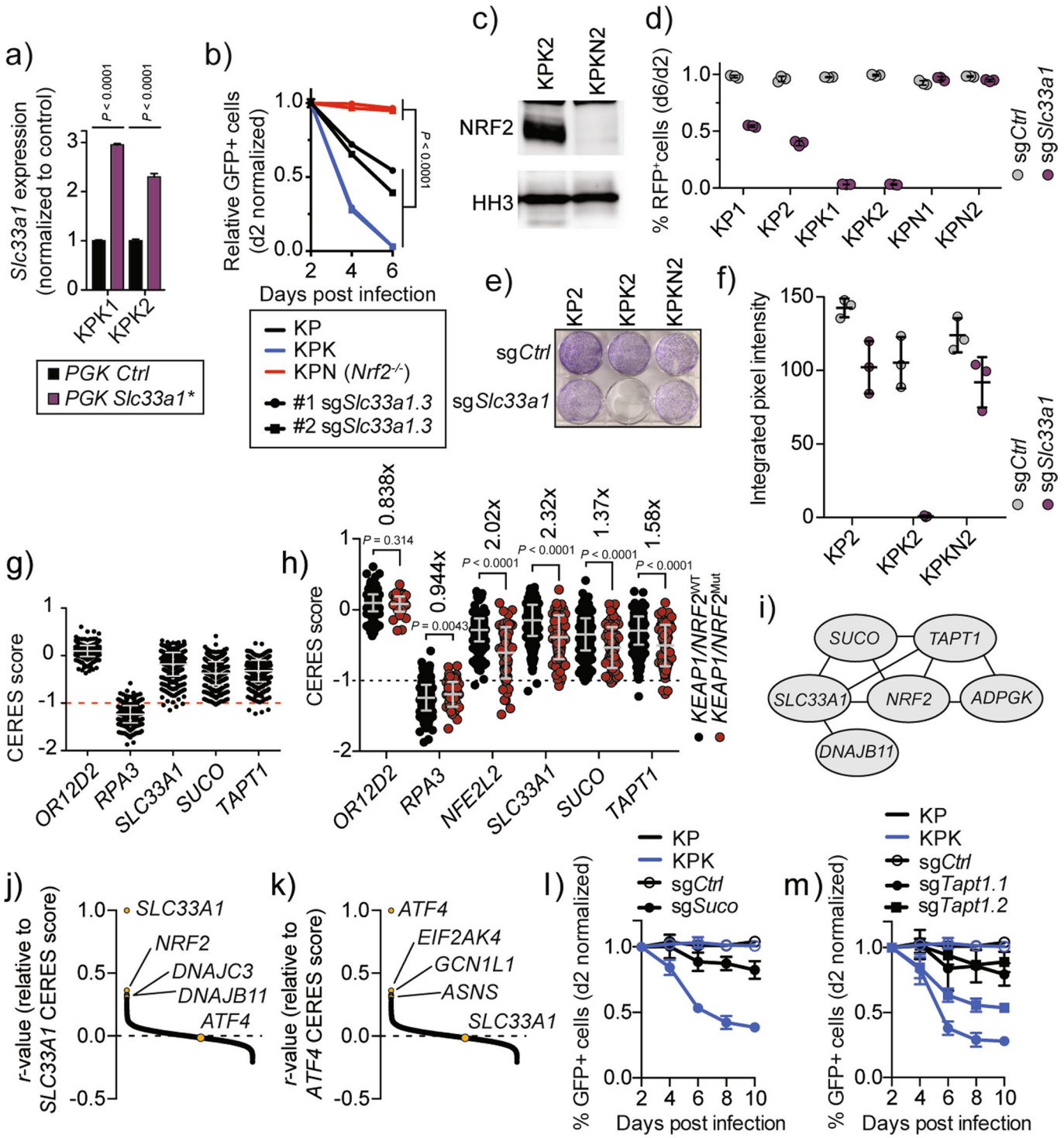

Extended Data Fig. 3 | See neext page for caption.

Extended Data Fig. 3 | *Slc33a1* dependency is abrogated in *Nrf2*-deficient cell lines and dependency is recapitulated across large human cancer cell line CRISPR-screens. a, *Slc33a1* expression quantified by qPCR in cells transduced with sgRNA-resistant cDNA (*) overexpression constructs. Bars represent mRNA expression normalized to *Actb* then to *PGK Ctrl* samples, and the error bars represent mean ± s.d. from the mean across $n = 4$ independent experiments. *P* values were determined by unpaired two-tailed Student's *t*-test. **b**, Fluorescence competition assay plot displays %RFP + cells marking sg*Ctrl* or sg*Slc33a1* infected cells over time. This experiment was performed once with $n = 4$ biologically independent samples obtained from two independent cell lines per genotype that were tested with two independent sgRNAs. *P* values were determined by two-way ANOVA with Tukey's *post-hoc* multiple comparisons test. **c**, NRF2 western blot of KPK2 and a mixed population of pUSEPR-sg*Nrf2* KPK cells (KPKN2). Histone H3 was used as a loading control. Gel has been cropped to remove non-relevant cell lines and nonspecific NRF2 bands. **d**, Fluorescence competition assay plot displays day 2 normalized %RFP + cells marking sg*Ctrl* or sg*Slc33a1* infected cells over time. Data are representative of $n = 3$ independent culture wells per cell line per sgRNA. **e**, Colony formation assay of the indicated cell lines infected with sg*Ctrl* or sg*Slc33a1*. Data from $n = 3$ independent culture wells per cell line per sgRNA. **f**, Quantified colony formation assay via the integrated pixel density assessed by ImageJ software. Related to (**e**). Data are representative of $n = 3$ independent culture wells per cell line per sgRNA. **g**, CERES normalized scores obtained across all cell lines. Dotted red line represents the median CERES scores of all core-essential genes defined by the DepMap consortium (19Q2, $n = 563$ cell lines). **h**, CERES normalized scores obtained across *KEAP1/NRF2*-mutant or wild-type cancer cell lines ($n = 563$ total cells). Values above comparison denote the fold change relative to the average CERES score of the wild-type group. *P* values were determined by unpaired two-tailed Student's *t*-test. **i**, Co-dependencies arising from the DepMap dataset cluster *NRF2* with *SLC33A1, SUCO, TAPT1, DNAJBL11* and *ADPGK*. Each node depicts a gene. Connecting lines indicate a direct co-dependency shared between each node (ref. [28]). **j**,**k**, Waterfall plot of the rank ordered Pearson correlation coefficient between (**j**) *SLC33A1* CERES scores versus or (**k**) *ATF4* CERES scores versus all genes screened in the DepMap consortium (19Q2, $n = 563$ total cells). **l**,**m**, Fluorescence competition assays of sgRNA infected cells. Plot displays day 2 normalized %GFP + cells marking (**l**) sg*Ctrl* or sg*Suco* edited or (**m**) sg*Ctrl* or sg*Tapt1* edited cells. Data are representative of $n = 3$ independent culture wells per cell line per sgRNA and representative of three independent experiments with similar results. All error bars depicted represent mean ± s.d. unless otherwise stated. Data from a single experiment are shown in **c**, **d**, **e**, and **f** are representative of two independent experiments with similar results. Data for experiments **a, b, d, l** and **m** are available as source data (Source_Data_Extended_Data_1; Source_Data_Extended_Data_2).

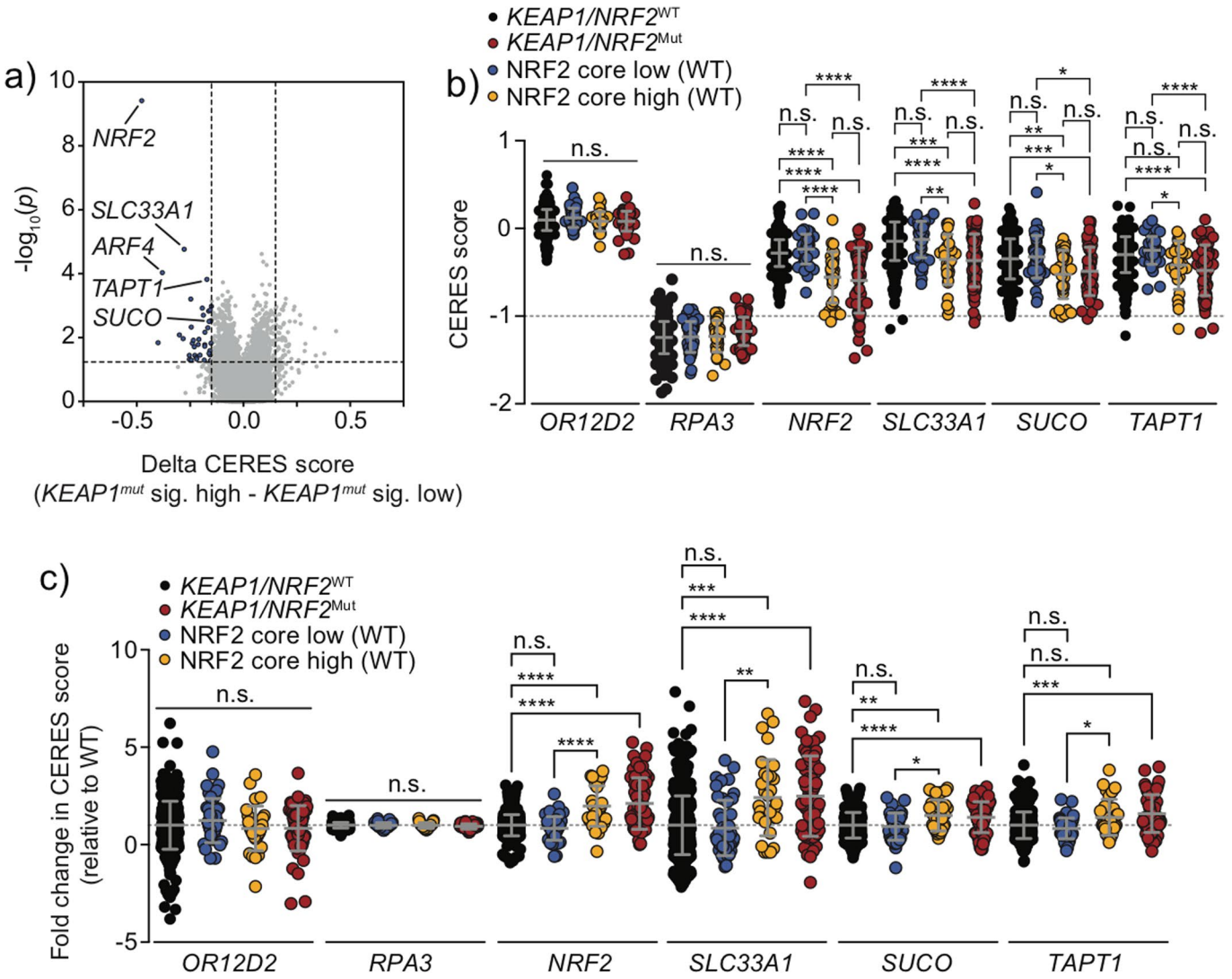

Extended Data Fig. 4 | NRF2 transcriptional states positively correlate with *SLC33A1* dependency, independently of *KEAP1* or *NRF2* mutation status. **a**, Differential CERES scores between *KEAP1*-mutant signature high-ranking cell lines ($n = 42$) versus low-ranking cell lines ($n = 32$) from ref. [64]. Horizontal dotted line represents *P* value significance cut-off ($P < 0.05$; unpaired two-sided Student's *t*-test). Each dot represents the differential gene score per gene. Blue dots represent genes that pass all set threshold values. **b**, Graph representing the median CERES score of the indicated genes across 558 cell lines ranked by the NRF2 core gene set high-ranking cell lines ($n = 31$) versus low-ranking cell lines ($n = 45$) from the DepMap that did not have annotated *NRF2/KEAP1* mutations or the remaining cells that were in either high- or low-ranking category and annotated as *NRF2/KEAP1*-wild-type ($n = 424$) or mutant ($n = 63$). Each dot represents the CERES score observed (ref. [64]). Dotted line represents the median CERES scores of all core-essential genes defined by the DepMap consortium. *OR12D2, P* = 0.5599; *RPA3, P* = 0.0504. **c**, Fold change of the data plotted in (**b**). Values are relative to the average of CERES score of the *NRF2/KEAP1*-wild-type cohort for each gene. *OR12D2, P* = 0.5599; *RPA3 P* = 0.0504. *P*-values in (**b**) and (**c**) were determined by Kruskal-Wallis test with Dunn's multiple comparisons testing. All error bars represent mean ± s.d. $^{*}P < 0.05$, $^{**}P < 0.01$, $^{***}P < 0.001$, $^{****}P < 0.0001$, n.s. = not significant.

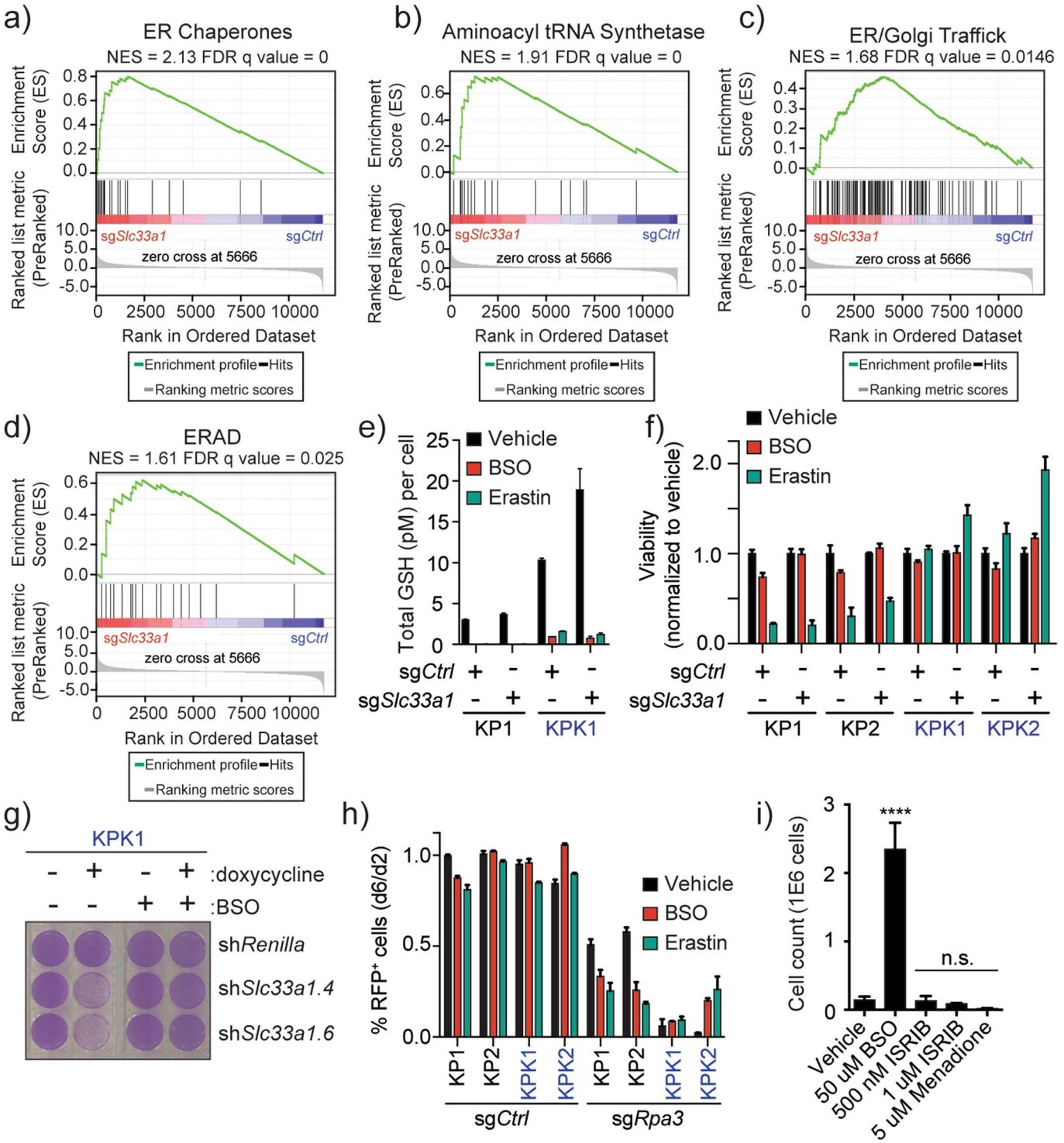

Extended Data Fig. 5 | *Slc33a1* loss promotes UPR transcriptional signatures and GSH synthesis inhibitors rescue *Slc33a1*-dependency. a-d, GSEA enrichment plots of conserved ER stress response signatures (ER chaperones FDR = 0.0; Aminoacyl tRNA synthetase FDR = 0.0; ER/Golgi traffic FDR = 0.0146; ERAD FDR = 0.025). Analysis derived from a single experiment from KP-sg*Ctrl*, KP-sg*Slc33a1*, KPK-sg*Ctrl*, KPK-sg*Slc33a1* samples. **e**, GSH concentrations measured in cells treated with or without 48 hours of (25 μM) BSO or (780 nM) Erastin. Data are representative of $n = 3$ independent culture wells per cell line per sgRNA. **f**, Viability of cells infected with sgRNAs and treated with or without 48 hours of BSO and Erastin as in (**e**). Viability was measured using cell-titer Glo. Data are representative of $n = 3$ independent culture wells per cell line per sgRNA per treatment condition. **g**, Colony formation assay of KPK1 cells transduced with LVt-TSTOP vectors expressing sh*Renilla* or sh*Slc33a1*. **h**, Day 2 normalized fluorescence competition assays of 50 μM BSO or 1 μM Erastin treated pUSEPR-infected KP or KPK isogenic cell lines expressing sg*Ctrl* or sg*Rpa3*. Data are representative of $n = 3$ independent culture wells per cell line per sgRNA. **i**, Total cell counts of KPK-*Slc33a1* knockout cells treated with indicated conditions 7 days post infection. Data are representative of $n = 3$ independent experiments. *P* values were determined by ANOVA with Dunnet's multiple comparisons testing. All error bars depicted represent mean ± s.d. $^{*}P < 0.05$, $^{**}P < 0.01$, $^{***}P < 0.001$, $^{****}P < 0.0001$, n.s. = not significant. Data from a single experiment are shown in **e**, **f**, **g**, and **h** are representative of two independent experiments with similar results. Data for experiments **e, f, h** and **i** are available as source data (Source_Data_Extended_Data_1; Source_Data_Extended_Data_3).

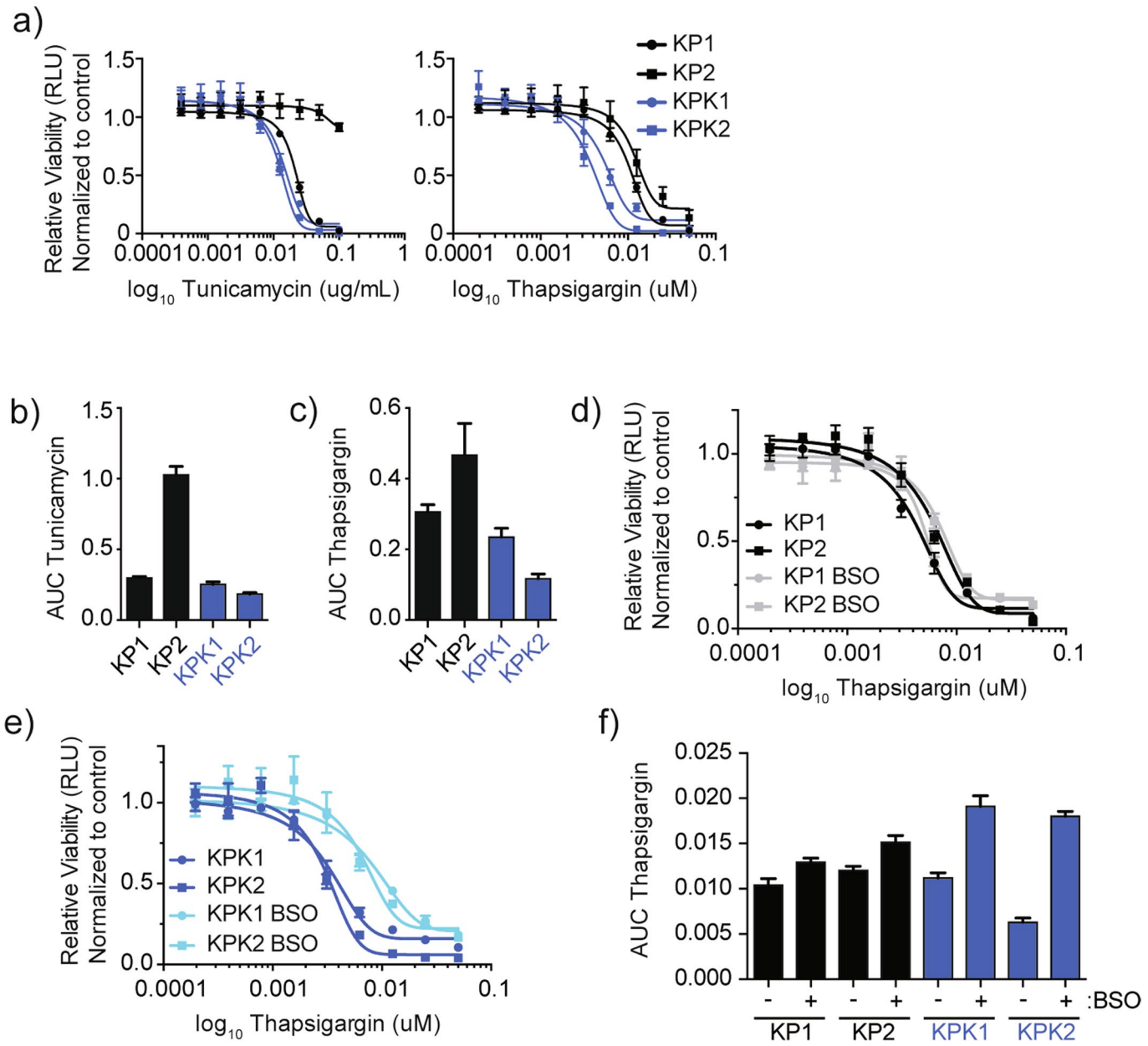

Extended Data Fig. 6 | *Keap1*-mutant cells are sensitized to chemical inducers of the UPR. a, Left: Dose response curve of KP and KPK isogenic pairs with tunicamycin for 48 hours. Right: Dose response curve of KP and KPK isogenic pairs with thapsigargin for 48 hours. Data are representative of $n=3$ independent culture wells per cell line per sgRNA. **b**, Area under the curve (AUC) analysis of tunicamycin treated cells as in (**a**). Data are representative of $n=3$ independent culture wells per cell line per sgRNA. **c**, AUC analysis of thapsigargin treated cells as in (**a**). Data are representative of $n=3$ independent culture wells per cell line per sgRNA. **d**, Dose response curve of BSO co-treated (50 μM) or untreated KP cell lines with thapsigargin for 48 hours. Data are representative of $n=3$ independent culture wells per cell line per sgRNA. **e**, Dose response curve of BSO co-treated (50 μM) or untreated KPK cell lines with thapsigargin for 48 hours. Data are representative of $n=3$ independent culture wells per cell line per sgRNA. **f**, AUC analysis of thapsigargin treated cells pretreated with 50 μM BSO as in (**h**) and (**i**). Data are representative of $n=3$ independent culture wells per cell line per sgRNA. All experiments denoted above are representative of $n=3$ parallel infections unless otherwise stated. All error bars depicted represent mean ± s.d. Data from a single experiment are shown in **a**-**f** are representative of two independent experiments with similar results. Data for experiments **a, d** and **e** are available as source data (Source_Data_Extended_Data_5).

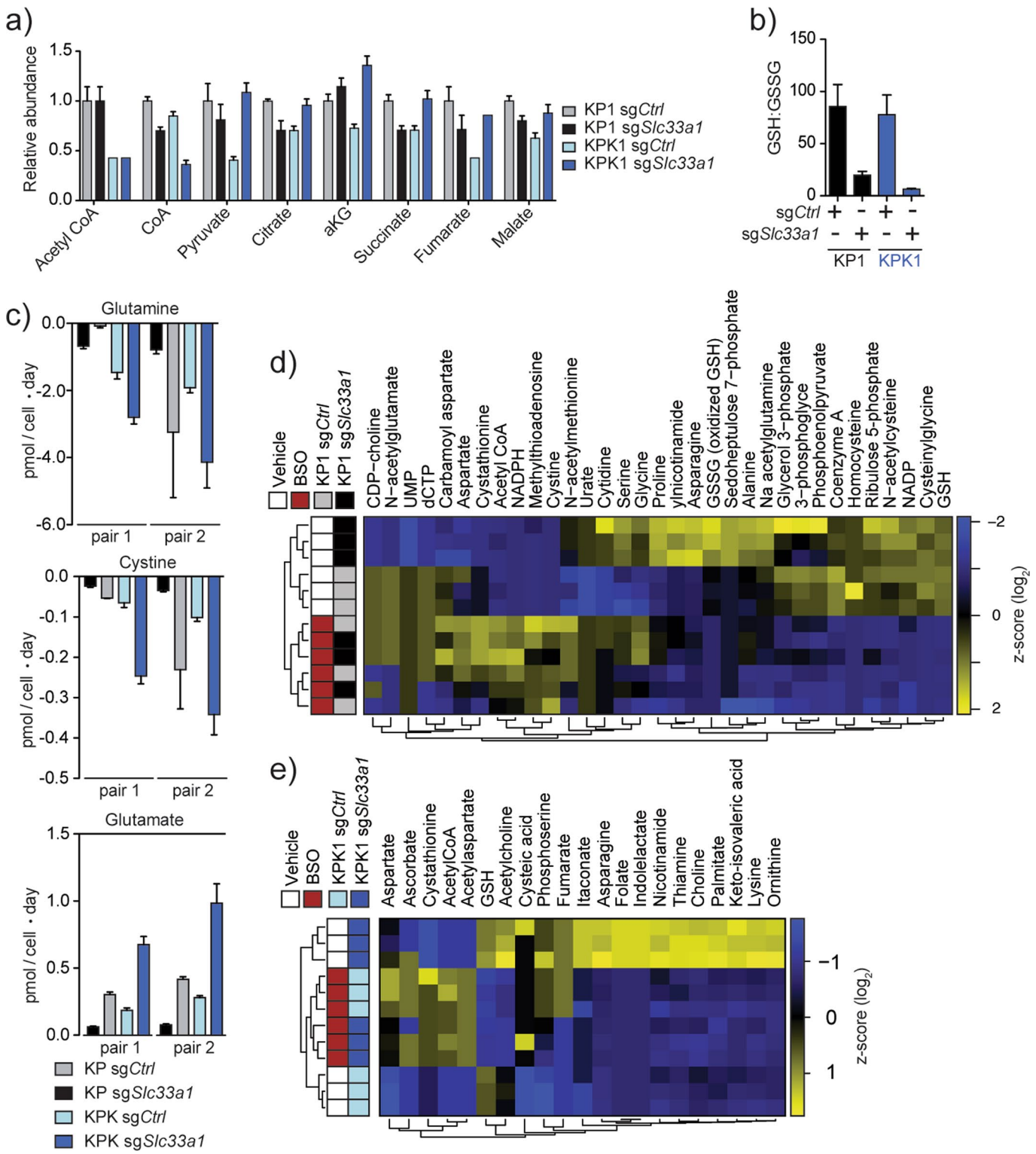

Extended Data Fig. 7 | *Slc33a1* loss results in broad metabolic changes that are rescued with BSO treatment. a, Relative abundance of detected TCA cycle-related metabolites across the depicted cell lines. Data is normalized by cell counts for each cell line. Data are representative of $n = 3$ independent culture wells per cell line per sgRNA. **b**, LC/MS detected GSH:GSSG ratios. Data are representative of $n = 3$ independent culture wells per cell line per sgRNA. **c**, GC/MS glutamine, cystine, and glutamate secretion in KP and KPK isogenic pairs. Data are representative of $n = 3$ independent culture wells per cell line per sgRNA. **d**, Unsupervised clustering of all detectable polar metabolites in KP1 cells transduced with sg*Ctrl* or sg*Slc33a1* in either vehicle or BSO treated conditions. Each row represents a different metabolite. Each column represents a different sample. Each cell line condition was completed across independent culture wells per cell line per sgRNA. Data are normalized by cell counts for each cell line. **e**, Unsupervised clustering of all detectable polar metabolites in KPK1 cells transduced with sg*Ctrl* or sg*Slc33a1* in either vehicle or BSO treated conditions. Data collected as in (**d**). Each column represents a different sample. Data is normalized by cell counts for each cell line. All error bars depicted represent mean ± s.d. All data shown above are from a single mass-spectrometry experiment.

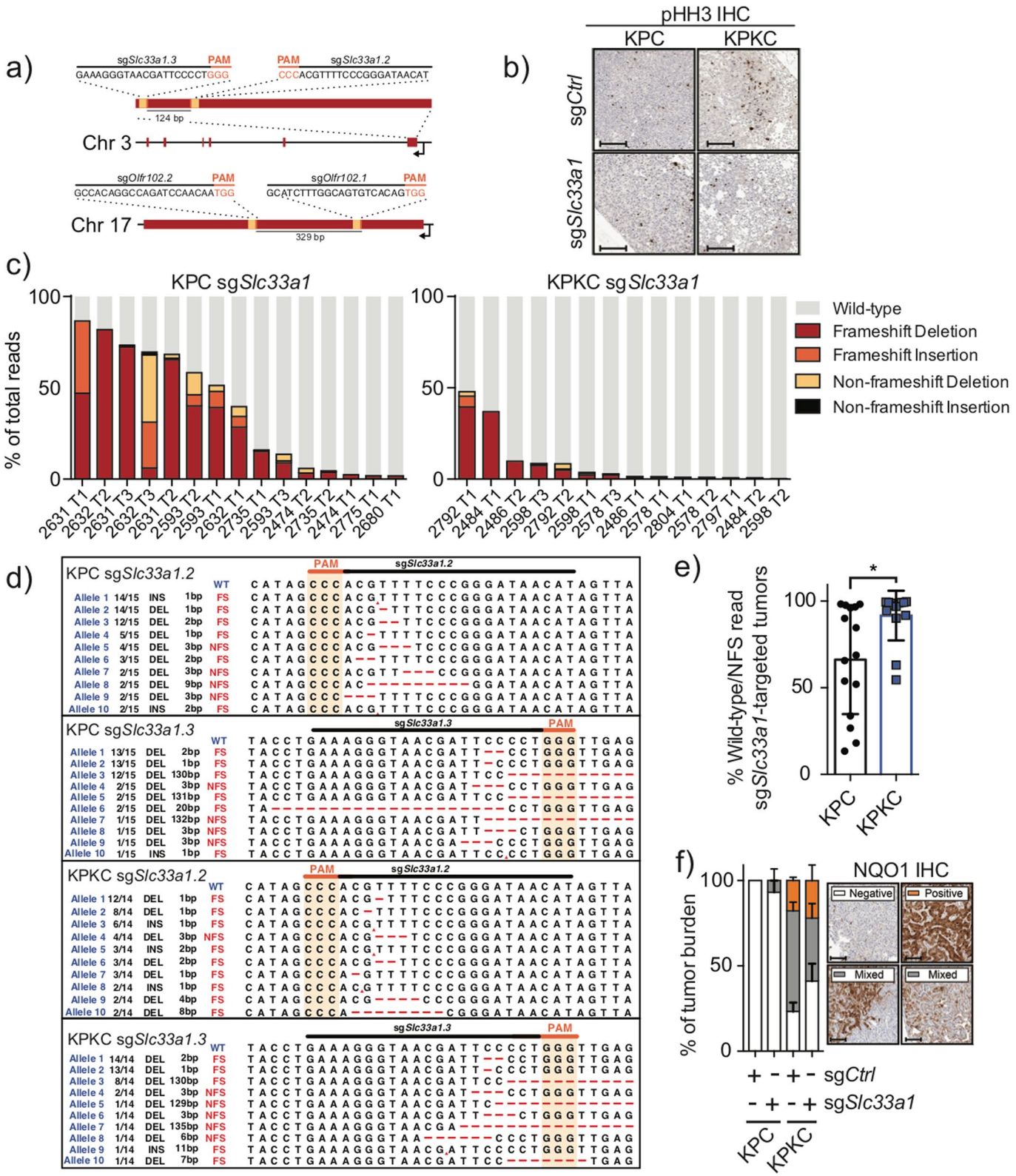

Extended Data Fig. 8 | See neext page for caption.

Extended Data Fig. 8 | *In vivo* validation of *Slc33a1* as a *Keap1*-mutant-specific vulnerability in a *Kras*-driven-*Keap1*-mutant GEMM of LUAD. **a**,Schematic representing sgRNA genomic binding sites for *Slc33a1* (top) and *Olfr102* (bottom; sg*Ctrl*). Distance between predicted cut-sites is denoted below the locus map. **b**,Representative images from pHH3 stained tumor bearing lung sections of the indicated samples. Scale bars indicate 100 μm. Number of mice analyzed by IHC equivalent to Fig. 6b. Tumor number across mice varies. Related to Fig. 6e. **c**,Fraction of mutant and wild-type reads within individual pUSEC-sg*Slc33a1* targeted tumors (KPC $n=15$; KPKC $n=14$) obtained 20 weeks post infection. FS = frameshift; NFS = non-frameshift. **d**,Representative alleles obtained from KPC (top) or KPKC (bottom) from plucked tumors 20 weeks post infection with pUSEC dual sgRNA lentiviruses expressing sg*Slc33a1.2* and sg*Slc33a1.3*. Plot summarizes the mutational analyses of locus-specific deep sequencing showing the *Slc33a1* wild-type locus containing the sg*Slc33a1.2* or sg*Slc33a1.3* binding site (black) and protospacer-adjacent motif (PAM) sequence (orange) along with representative mutant alleles. Dashes indicate deletion events and red arrows indicate insertion event. **e**, Mean number of wild type and non-frameshift (NFS) reads from pUSEC-sg*Slc33a1* lentiviral-infected KPC (mean of $n=15$ tumors from 7 mice) and KPKC mice (mean of $n=14$ tumors from 7 mice). *P* values were determined by unpaired two-tailed Student's *t*-test. **f**, IHC of the NRF2 target, NQO1, from tumor bearing lung sections of the indicated samples. Stacked bar chart represents the average distribution of NQO1 positive, mixed, or negative tumors. Representative images of NQO1 staining (right). Number of mice analyzed by IHC equivalent to Fig. 6b. Tumor number across mice varies. Related to Fig. 6h (Scale bar = 100 um). All error bars depicted represent mean ± s.d.

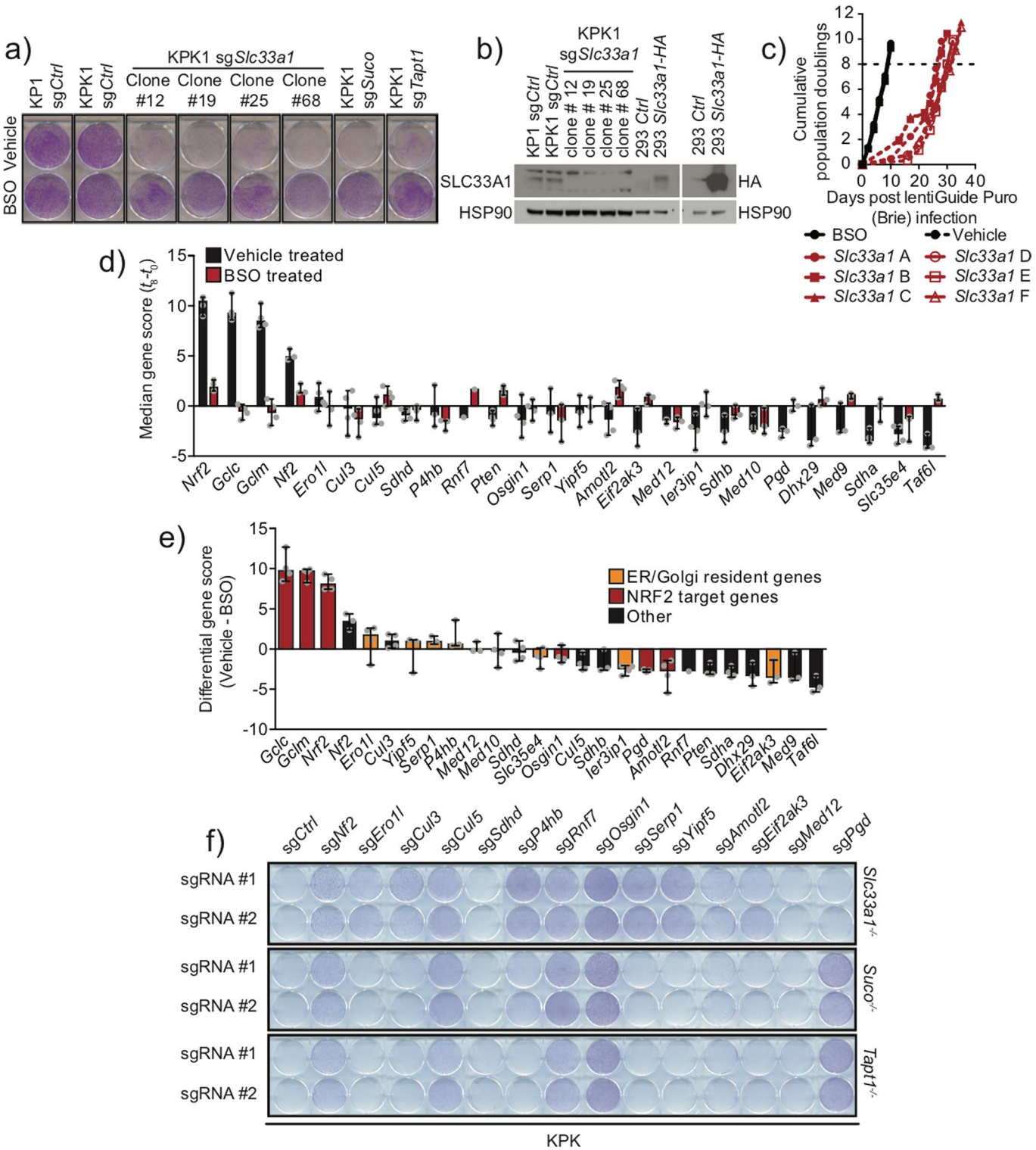

Extended Data Fig. 9 | See neext page for caption.

Extended Data Fig. 9 | Genome-wide CRISPR screen identifies multiple suppressors of *Slc33a1* dependency. a, Colony formation assay of the indicated cell lines grown in the presence or absence of 50 μM BSO for 7 days. Results representative of $n = 3$ independent culture wells per cell line per treatment condition across KPK1 *Slc33a1* KO clones ($n = 5$) or KPK1 *Suco* ($n = 1$) or KPK1 *Tapt1* KO ($n = 1$) clones infected in parallel. **b**, Western blot validation of *Slc33a1* knockout. 293Ts overexpressing HA-tagged SLC33A1 serve as a positive control for antibody detection and validation. Results representative of $n = 2$ independent experiments. Gel has been cropped to separate KP/KPK cells away from 293T samples run on the same gel. **c**, Cumulative population doublings of *Slc33a1* knockout cell pools infected with Brie library in replicates and placed in either BSO ($n = 6$ independent culture wells per cell line per condition) or vehicle-treated ($n = 3$ independent culture wells per cell line per condition) conditions infected in parallel. **d**, Median GSs of the top enriched genes from Brie library-infected KPK-*Slc33a1* knockout cells. Error bars represent the range of the data from a single experiment for detected sgRNAs across $n = 3$ to 4 independent sgRNAs per gene per sample (Exception: $n = 1$ for sg*Rnf7* per condition). **e**, Median differential gene scores of the top enriched genes from Brie library-infected KPK-*Slc33a1* knockout cells. Error bars represent the range of the data from a single experiment for detected sgRNAs across $n = 3$ to 4 independent sgRNAs per gene per sample (Exception: $n = 1$ for *Rnf7*). **f**, Validation of the top enriched gene candidates by colony formation assay. KPK-*Slc33a1*, -*Suco*, or -*Tapt1* knockout cells were infected with two top-scoring sgRNAs targeting the genes listed in vehicle treated conditions. Representative images from $n = 3$ independent culture wells per cell line per sgRNA. Related to Fig. 7e. Data from a single experiment are shown in **a**, **b**, and **f** are representative of two independent experiments with similar results. Unmodified gel images for **b** are available as source data (Source_Data_Fig_2).

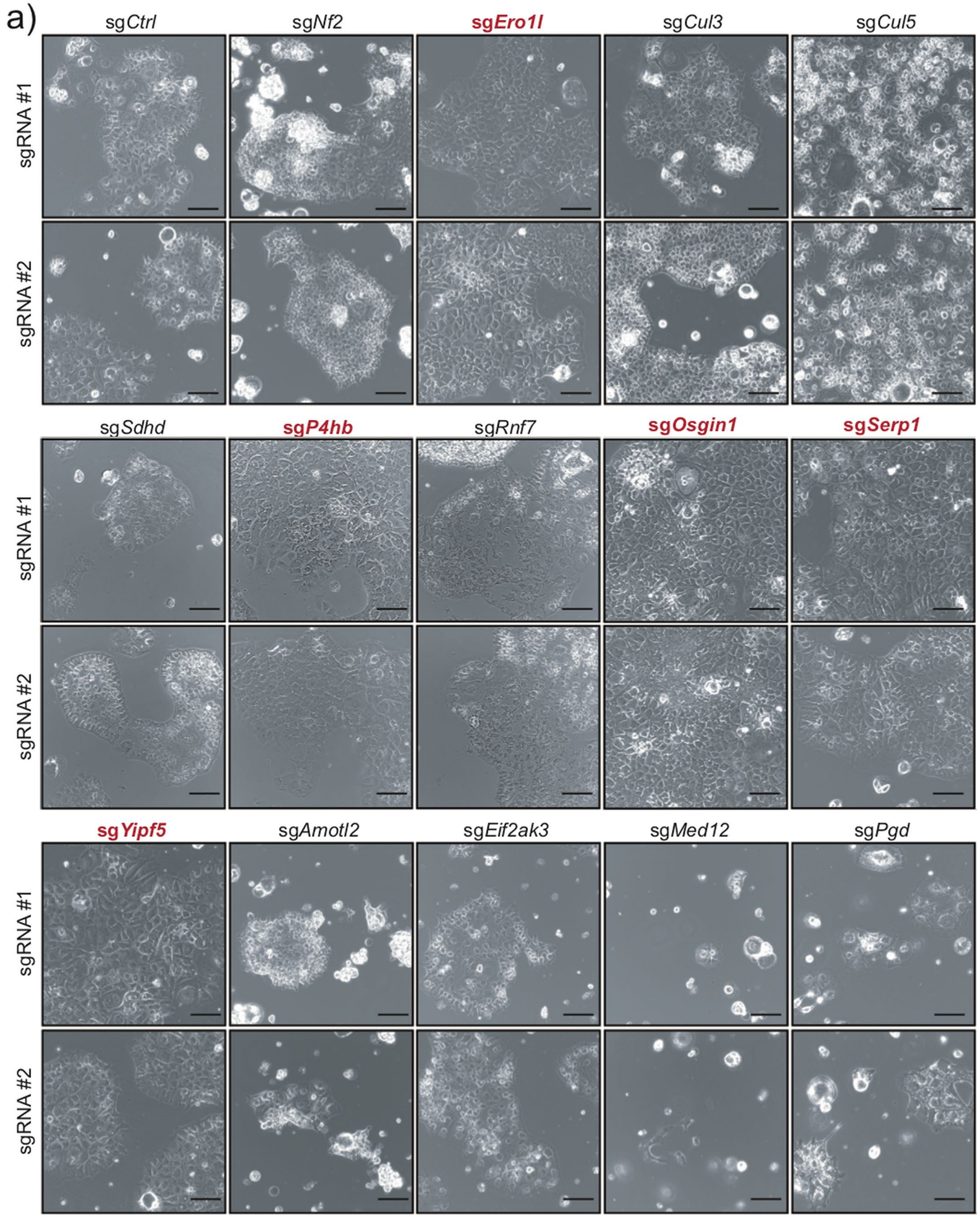

Extended Data Fig. 10 | Genes targeting ER-resident genes rescue *Slc33a1* knockout cellular phenotypes. a, Microscopy of KPK-*Slc33a1* knockout cells infected with the top scoring sgRNAs targeting the listed genes. sgRNAs listed in red denote cells in which the blebbing phenotype associated with *Slc33a1* loss was rescued relative to sg*Ctrl* cells. Scale bar = 100 μm. Representative images from $n = 3$ independent experiments. Related to Fig. 7e and Extended Data Fig. 9f.

nature research

Corresponding author(s): Tyler Jacks

Last updated by author(s): 05/09/2020

Reporting Summary

Nature Research wishes to improve the reproducibility of the work that we publish. This form provides structure for consistency and transparency in reporting. For further information on Nature Research policies, see Authors & Referees and the Editorial Policy Checklist.

Statistics

For all statistical analyses, confirm that the following items are present in the figure legend, table legend, main text, or Methods section.

n/a	Confirmed	
☐	☒	The exact sample size (*n*) for each experimental group/condition, given as a discrete number and unit of measurement
☐	☒	A statement on whether measurements were taken from distinct samples or whether the same sample was measured repeatedly
☐	☒	The statistical test(s) used AND whether they are one- or two-sided *Only common tests should be described solely by name; describe more complex techniques in the Methods section.*
☒	☐	A description of all covariates tested
☐	☒	A description of any assumptions or corrections, such as tests of normality and adjustment for multiple comparisons
☐	☒	A full description of the statistical parameters including central tendency (e.g. means) or other basic estimates (e.g. regression coefficient) AND variation (e.g. standard deviation) or associated estimates of uncertainty (e.g. confidence intervals)
☐	☒	For null hypothesis testing, the test statistic (e.g. *F*, *t*, *r*) with confidence intervals, effect sizes, degrees of freedom and *P* value noted *Give P values as exact values whenever suitable.*
☒	☐	For Bayesian analysis, information on the choice of priors and Markov chain Monte Carlo settings
☐	☒	For hierarchical and complex designs, identification of the appropriate level for tests and full reporting of outcomes
☐	☒	Estimates of effect sizes (e.g. Cohen's *d*, Pearson's *r*), indicating how they were calculated

Our web collection on statistics for biologists contains articles on many of the points above.

Software and code

Policy information about availability of computer code

Data collection	Bioinformatic analysis were performed using open-source software, including RSEM version 1.2.12 (ref. 76), JADE version 1.1.0, Annovar versions 2016-02-01 (ref. 73), SeqAn version 2.0.1 (ref. 74), SSW version 0.1.4, as well as in-house scripts in R that are available from the corresponding author on reasonable request.
Data analysis	Bioinformatic analysis were performed using open-source software, including RSEM version 1.2.12 (ref. 76), JADE version 1.1.0, Annovar versions 2016-02-01 (ref. 73), SeqAn version 2.0.1 (ref. 74), SSW version 0.1.4, as well as in-house scripts in R that are available from the corresponding author on reasonable request.

For manuscripts utilizing custom algorithms or software that are central to the research but not yet described in published literature, software must be made available to editors/reviewers. We strongly encourage code deposition in a community repository (e.g. GitHub). See the Nature Research guidelines for submitting code & software for further information.

Data

Policy information about availability of data

All manuscripts must include a data availability statement. This statement should provide the following information, where applicable:

- Accession codes, unique identifiers, or web links for publicly available datasets
- A list of figures that have associated raw data
- A description of any restrictions on data availability

Bulk RNA-seq data have been deposited into the NCBI Gene Expression Omnibus (GEO) database (http://www.ncbi.nlm.nih.gov/geo/) under accession number GSE145945. CRISPR screen and target locus sequence datasets have been submitted to the Sequence Read Archive (SRA) and are available under BioProject ID PRJNA611102. Mass spectrometry data have been deposited in Metabolights with the primary accession code MTBLS1647 Numerical source data for Main and Extended Data Figures are provided as Source Data Extended Data files 1-6 (Source_Data_Extended_Data_1- Source_Data_Extended_Data_2- Source_Data_Extended_Data_3- Source_Data_Extended_Data_4- Source_Data_Extended_Data_5- Source_Data_Extended_Data_6). All other data supporting the findings of this study are available from the corresponding author on reasonable request.

Field-specific reporting

Please select the one below that is the best fit for your research. If you are not sure, read the appropriate sections before making your selection.

☒ Life sciences ☐ Behavioural & social sciences ☐ Ecological, evolutionary & environmental sciences

For a reference copy of the document with all sections, see nature.com/documents/nr-reporting-summary-flat.pdf

Life sciences study design

All studies must disclose on these points even when the disclosure is negative.

Sample size	Sample sizes for each experiment are outlined in the figure legends for each corresponding sub-figure. For all experiments, at least 3 or more replicates/number of animals was used to determine statistical significance. All cell based assays are representative of independent experiments in which cells were infected and seeded into technical replicate conditions across independent experiments. Data represented by a single experiment are written in the figure legend along with a statement of reproducibility across independent experiments. For all animal studies, n > 3 mice were used for each experimental cohort per specified genotype. Total burden, grading analysis, and histopathological analyses were conducted on n > 3 mice per genotype. No statistical method was used to predetermine sample size. Sample sizes for mice were chosen depending on the experiment. For allografts, 3 mice with 2 tumors per flank result in relatively non-variable tumor sizes. For xenograft studies n > 5 mice used (10 tumors) as xenografts display increased variability relative to allografts. For autochthonous induction of lung tumors, two separate cohorts of 10 mice per infection group were used, as GEMMs yield the highest variability. Results from both independent GEMM experiments were combined and used for data analysis. For all cell line experiments, as previously stated, all are derived from n > 3 independent experiments unless otherwise stated. Sample size was chosen due to the low inherent variability and high reproducibility of results between experiments. DGL Screen: KP1, KPK1, KP2, and KPK2 cell lines were infected once in a single experiment. As these data include enrichment and depletion across biologically distinct but isogenic cell lines (i.e. KP1 and KP2; KPK1 and KPK2), we opted to infect and screen at n = 1 per cell line. Genome-wide Screen (Brie): KPK-Slc33a1 KO clones were pooled and subsequently infected in parallel infections (n = 3) in media containing BSO. Cells from each replicate infection were split into three groups, 1) BSO maintained 2) BSO seeded and withdrawn 24 hours post seed, and 3) seed directly into vehicle treated conditions. Due to severe depletion of the library in the absence of BSO, all BSO withdrawn conditions were combined into one group for analysis post sequencing deconvolution and demultiplexing.
Data exclusions	Animals lacking detectable tumors by histopathology were excluded from the analysis to ensure all animals were successfully infected with pUSEC lentiviruses. No other data were excluded from any analysis.
Replication	All experiments were reproduced 2 or more times using the same experimental approach or in the case of mice or cells, use of two or more sgRNAs/shRNAs targeting Slc33a1, Arf4, Suco, Tapt1, Rpa3, or Olfr102 (Ctrl), each with a unique targeting sequence. For validation of the whole genome screen, two sgRNA sequences were used per candidate gene. For GEMM tumor burden analysis, the total number of mice used in the representative figures are derived from two separate cohorts of mice that were infected at different time points, but sacrificed at an equivalent time point post infection and tumor induction. For all experiments in which representative results are shown, all results were successfully replicated.
Randomization	Mice of the ages between 8-10 weeks of the correct genotypes were randomly selected, with no sex-bias, to be included in tumor initation studies. Post-mortem tumor burden was performed by a deep neural network (unpublished) developed by Thomas Westerling of Aiforia Technologies in collaboration with the Tammela and Jacks labs, and consultation with veterinarian pathologist Dr. Roderick Bronson. The algorithm performed consistently and with high correlation with human graders across multiple validation datasets independent of the training dataset.
Blinding	See above, all burden analysis and IHC was done in a blinded fashion, or performed via trained deep neural networks in which information on the genotype of the animal was excluded in the procedure and only assessed after the algorithm had completed. See Methods for more information.

Reporting for specific materials, systems and methods

We require information from authors about some types of materials, experimental systems and methods used in many studies. Here, indicate whether each material, system or method listed is relevant to your study. If you are not sure if a list item applies to your research, read the appropriate section before selecting a response.

Materials & experimental systems

n/a	Involved in the study
☐	☒ Antibodies
☐	☒ Eukaryotic cell lines
☒	☐ Palaeontology
☐	☒ Animals and other organisms
☒	☐ Human research participants
☒	☐ Clinical data

Methods

n/a	Involved in the study
☒	☐ ChIP-seq
☐	☒ Flow cytometry
☒	☐ MRI-based neuroimaging

Antibodies

Antibodies used

The following antibodies were used for immunoblotting: anti-GAPDH (Santa Cruz, sc-25778, 1:500), anti-HSP90 (BD, #610418, 1:10,000), anti-NRF2 (Santa-Cruz, sc-722, 1:200), anti-KEAP1 (CST, #8047, 1:1000), anti-GCLC (Santa Cruz, sc-22755, 1:200). anti-p62 (CST #23214, 1:1000), anti-LC3 (CST #12741, 1:1000), anti-BECLIN (CST #3495, 1:1000), anti-pS6K T421/424 (CST #9204, 1:1000), anti-BiP (CST 3177, 1:1000), anti-FLAG (CST #14793, 1:1000), anti-HH3 (CST #4499, 1:1000), anti-GCN2 (CST #65981S, 1:1000), anti-PERK (CST #5683S, 1:1000), anti-ATF4 (CST #11815S, 1:1000), anti-eIF2a (CST #5324S, 1:2000), anti-phospho-eIF2a S51 (CST #3398S, 1:1000), anti-SLC33A1 (Sigma HPA042430, 1:1000), Anti-Mouse HRP (CST #7076, 1:10,000), Anti-Rabbit HRP (CST #7074, 1:10,000).

Validation

All antibodies used in this study had been previously published or validated using engineered knock-out or shRNA-mediated knock-down cell lines. Anti-NRF2 antibody was validated in cell lines treated with vehicle or the oxidant Sulforaphane. Anti-SLC33A1 antibody validated using HEK293T cells overexpressing C-terminally HA tagged Slc33a1. All other antibodies were used in accordance with manufacturer suggested dilutions and protocols. All antibodies for IHC used as stated previously (ref. 14).

Eukaryotic cell lines

Policy information about cell lines

Cell line source(s)

Murine cell lines used in this study are derived from KP tumor bearing mice. These mice were donated by Leny Gocheva of the Jacks lab and have been described and published. KP1 and KPK1 cell lines correspond to KP2 and KPK1 cell lines from ref. 14 (clones derived from parental line KP cell line #1233 T6). This manuscript's KP2 and KPK2 are new and unpublished engineered cell lines derived from parental KP cell line (KP #1234 T4) gifted by Leny Gocheva as previously stated.
A549, H2009, H441, and HEK293T were acquired from ATCC.

Authentication

Murine cell lines are derived by the Jacks lab from pre-genotyped mice. Human cell lines were acquired directly from the ATCC. Cell lines used in this study have not been authenticated via SNP testing as they were freshly ordered from ATCC prior to use in this manuscript.

Mycoplasma contamination

All cell lines used in this study were tested for Mycoplasma contamination and repeated routinely every 6 months. None of the cell lines used in this study tested positive for Mycoplasma contamination.

Commonly misidentified lines
(See ICLAC register)

No

Animals and other organisms

Policy information about studies involving animals; ARRIVE guidelines recommended for reporting animal research

Laboratory animals

C57BL/6:SV129 mixed background males and females of 8-10 weeks were used for autochthonous development of tumors in the KP or KPK GEMMs initiated by lentiviral pUSEC vectors expressing Cre and sgCtrl (sgOlfr102) or sgSlc33a1 tandem dual guide RNAs.

Nude mice of 6-8 weeks (Jackson labs J:NU) were used for allograft and xenograft experiments (subcutaneous; female mice only).

Please see materials and methods section for more information.

Wild animals

No wild animals were used in this study

Field-collected samples

No field-collected samples were collected for this study

Ethics oversight

All animal studies described in this study were approved by the MIT Institutional Animal Care and Use Committee.

Note that full information on the approval of the study protocol must also be provided in the manuscript.

Flow Cytometry

Plots

Confirm that:

☒ The axis labels state the marker and fluorochrome used (e.g. CD4-FITC).

☒ The axis scales are clearly visible. Include numbers along axes only for bottom left plot of group (a 'group' is an analysis of identical markers).

☒ All plots are contour plots with outliers or pseudocolor plots.

☒ A numerical value for number of cells or percentage (with statistics) is provided.

Methodology

Sample preparation	See materials and methods
Instrument	Guava easyCyte HT flow cytometer (Millipore)
Software	Guava easyCyte software
Cell population abundance	Please see Methods
Gating strategy	Please see Methods

☒ Tick this box to confirm that a figure exemplifying the gating strategy is provided in the Supplementary Information.